2013

Time Domain Simulation of Novel Photovoltaic Materials

Haejun Chung
Purdue University

Graduate School ETD Form 9
(Revised 12/07)

PURDUE UNIVERSITY
GRADUATE SCHOOL
Thesis/Dissertation Acceptance

This is to certify that the thesis/dissertation prepared

By Haejun Chung

Entitled
Time Domain Simulation of Novel Photovoltaic Materials

For the degree of Master of Science in Electrical and Computer Engineering

Is approved by the final examining committee:

PETER A. BERMEL
Chair

DAVID B. JANES

MUHAMMAD A. ALAM

To the best of my knowledge and as understood by the student in the *Research Integrity and Copyright Disclaimer (Graduate School Form 20)*, this thesis/dissertation adheres to the provisions of Purdue University's "Policy on Integrity in Research" and the use of copyrighted material.

Approved by Major Professor(s): PETER A. BERMEL

Approved by: M. R. Melloch 11-25-2013
Head of the Graduate Program Date

TIME DOMAIN SIMULATION WITH NOVEL PHOTOVOLTAIC MATERIALS

A Thesis

Submitted to the Faculty

of

Purdue University

by

Haejun Chung

In Partial Fulfillment of the

Requirements for the Degree

of

Master of Science in Electrical and Computer Engineering

December 2013

Purdue University

West Lafayette, Indiana

I would like to thank Prof. Bermel for the great experience under his guidance for the past three semesters. I was constantly amazed by his deep understanding of physics and computer science. Whenever I faced difficulties while conducting my research, it was very encouraging to know that I could discuss any of questions over a wide range of scientific issues with him. In fact, his knowledge and his excellent advices have guided my research in the right direction. I hope he will still be my advisor in my Ph.D. program at Purdue University.

I also thank the professors on my Master's committee, Prof. Alam and Prof. Janes. it was very helpful to me to hear their opinions and insights in their respective fields during the examination period.

I thank Prof. Jung from Hanyang university, who was my advisor when I was an undergraduate student . He gave many opportunities to conduct research even though I was just a beginner at that time. Also, he suggested that I consider a very interesting research field, i.e., computational electromagnetics. My involvement in this research turned out to be a significant turning point in my professional development.

Finally, I thank my family for their love and support over the years. My mother, who has conducted research throughout her career, always has been a great role model. I offer my sincere thanks to my family for always believing in me and encoouraging me, even during the times that I was struggling with various difficulties.

TABLE OF CONTENTS

Page

LIST OF TABLES

LIST OF FIGURES

Figure Page

ABSTRACT

Chung, Haejun MSECE, Purdue University, December 2013. Time Domain Simulation With Novel Photovoltaic Materials. Major Professor: Peter Bermel.

Thin-film silicon-based solar cells have operated far from the Shockley-Queisser limit in all experiments to date. Novel light-trapping structures, however, may help address this limitation. Finite-difference time domain simulation methods offer the potential to accurately determine the light-trapping potential of arbitrary dielectric structures, but suffer from materials modeling problems. In this thesis, existing dispersion models for novel photovoltaic materials will be reviewed, and a novel dispersion model, known as the quadratic complex rational function (QCRF), will be proposed. It has the advantage of accurately fitting experimental semiconductor dielectric values over a wide bandwidth in a numerically stable fashion. Applying the proposed dispersion model, a statistically correlated surface texturing method will be suggested, and light absorption rates of it will be explained. In future work, these designs will be combined with other structures and optimized to help guide future experiments.

1. INTRODUCTION

Sunlight is one of the most promising sources of energy. It has been predicted that sunlight will be used to supply the world's energy requirements within the next 20 years [1]. The amount of solar power incident to the Earth is 10,000 times larger than the commercial energy used by every human on the planet [1]. However, the enormous potential of this resource cannot be realized by the current techniques of converting sunlight into electricity. In this thesis, a novel light trapping method is proposed to enhance the efficiency of current photovoltaic systems.

Recently, the solar cell industry has been growing at a very rapid pace. In the near future, the solar cell market, including modules and systems is expected to expanded to as much as 50 billion USD [1]. The majority of the solar cell market depends on by silicon-based technology [2]. However, the lack of an adequate supply of wafers has had a detrimental economic effect on the industry due to the fluctuating prices of the scarce wafers. This fact provides clear evidence of the importance of the development and utilization of thin film solar cells (TFSCs). The TFSCs have two major advantages over ordinary, wafer-based solar cell technology, i.e., they provide the same amount of energy for only $15 - 20\%$ of the cost. However, TFSCs have relatively lower maximum efficiencies. For example, one of the best CIGS-based solar cell operates at 20.3% efficiency, whereas a double-junction TFSC only has 12.5% stabilized efficiency [2].

1.1 Thin-Film Solar Cell

There are two major types of TFSC technologies, i.e., silicon thin-film solar cells and chemical-compound, thin-film solar cell(CIGS, CdTe). Between these two types, the silicon TFSC is more commonly used in the industry due to the availability of the

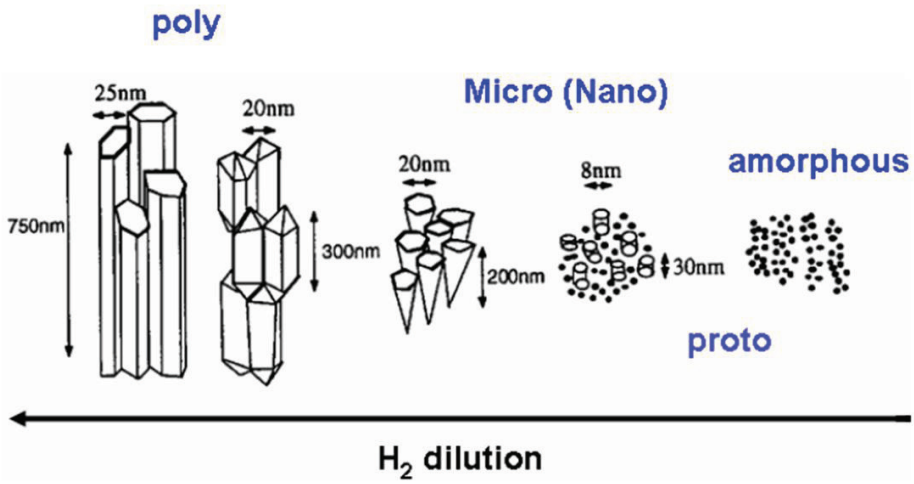

Fig. 1.1. Categorization of thin film type of silicon. [3]

mass-production technology referred to as TFT-LCD. Also, it has been proven that silicon does not have any harmful effect on the human body. As a result, the use of TFSCs is expected increase rapidly in the coming years [3].

The history of silicon TFSC began in 1969 when a manufacturing process called 'sputtering' was developed for amorphous silicon [3]. However, this process was considered to be an imperfect way to produce a TFSC, because the amorphous silicon-based thin films produced by the sputtering process had defects that are frequently observed in amorphous materials. At the 1969, the 'glow discharge' manufacturing process was developed and it significantly reduced the amount of defects produced in the amorphous silicon manufacturing process. The Sanyo Company developed an electronic calculator that contained a silicon TFSC, and this was the first commercial application of such a cell [3].

The deposition of a thin film of silicon is done with SiH_4 and H_2 using the plasma enhanced chemical vapor deposition(PECVD) method. Depending on the amount of H_2 gas, the thin film of silicon is categorized as poly silicon, micro(or nano) silicon and amorphous silicon. The amorphous silicon does not contain any crystal structure, and the arrangement of the atoms is totally random. Both the amorphous and crystalline

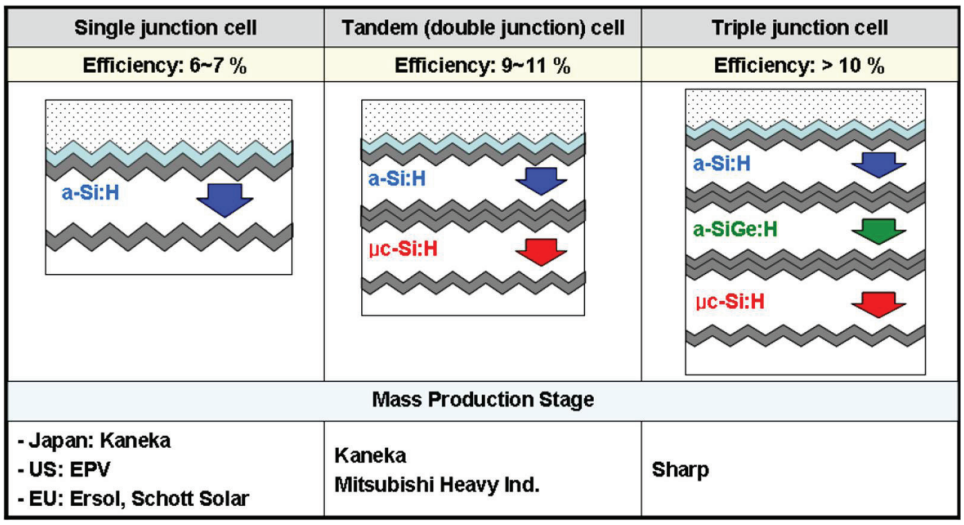

Fig. 1.2. Tandem cell structures and their mass production stage [3]

structures exist in the micro and nano crystalline silicon. In the latter type, the width of the crystal structure is around 20 nm. In other words, the poly-crystalline silicon does not have an amorphous structure, and the width of crystal is greater than 20 nm.

There have been three different generations of silicon-based TFSCs, and the first generation is called single-junction TFSCs. These solar cells have active materials consist of amorphous silicon or mirco silicon. This is the simplest structure, so manufacturing costs are relatively low. However, the efficiencies of such cells are only about 6 to 7% [4].

The second generation of silicon-based TFSCs is referred to as tandem cells or double-junction cells. These cells have about 9 to 11% efficiency, which is much better than that of the single-junction TFSCs. However, the increased manufacturing cost, caused by the complicated structure, is the main disadvantage. If one could make higher efficiency solar cells with low manufacturing cost using the tandem-cell structure, it would be a good business model. The third generation of TFSCs is called triple-junction cells. These cells have three layers, i.e., an amorphous silicon layer, an amorphous silicon-germanium layer, and a layer of micro crystalline silicon. The

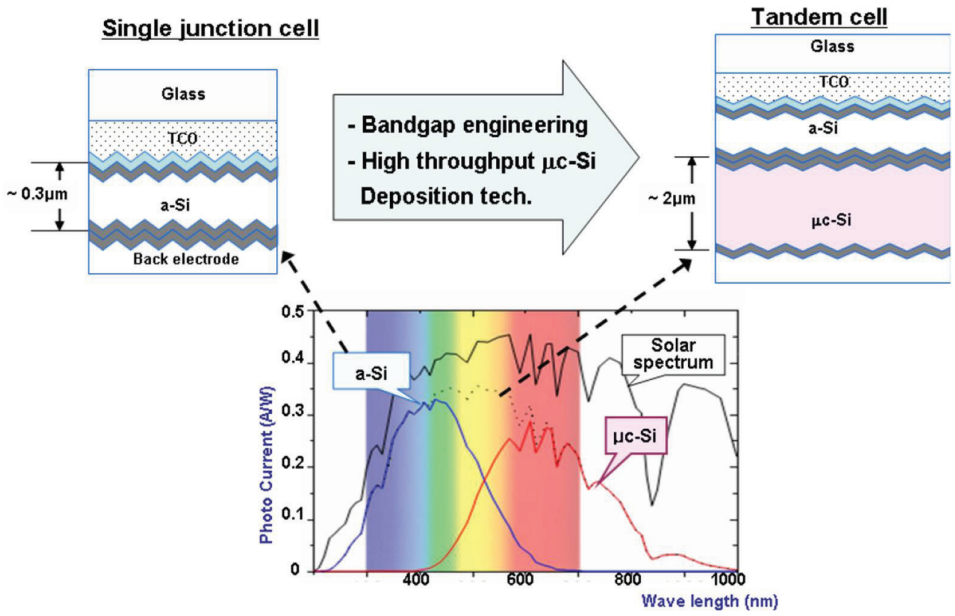

Fig. 1.3. Operation of a tandem cell with different band-gap materials [3]

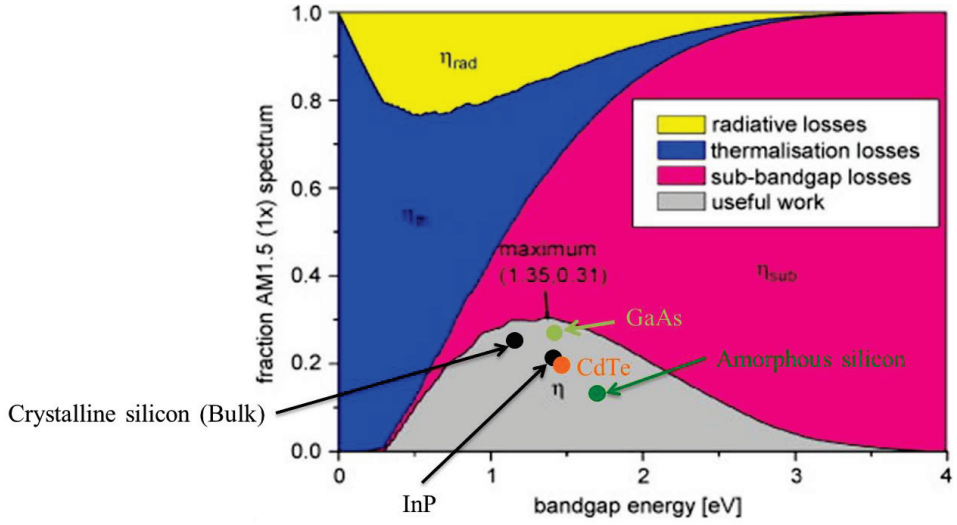

Fig. 1.4. Shockley and Queisser's limit in terms of band-gap [7]

triple junction cells provide a cell efficiency than can exceed 15%, but the original cost asks for the additional amorphous silicon germanium manufacturing process [5, 6].

1.2 Shockley and Queisser's limit

If we focus on the efficiency of a photovoltaic system, it is common to ask: "For the given TFSC material, what is the best design that can provide the most efficient conversion of solar energy?" The well-known theory developed by Shockley and Queisser provided the ultimate limit to a solar cell's energy conversion efficiency for a given material and given structure [7]. As shown in Fig. 1.4, the line drawn just above the grey region is Shockley and Queisser's limit in terms of the band gap of the materials. Fig. 1.4 also shows that the low band-gap material is dominated by thermalization losses and radiative losses as denoted by the blue and yellow regions, respectively. For high band-gap materials, sub-band-gap losses are dominant. Compared to other PV materials, such as GaAs and CdTe drawn in this figure, single-junction solar cells for a-Si operated far from the Shockley-Queisser limit. This means the green dot has additional room to shift upward. The concept that an a-Si, single-junction solar cell

can potentially achieve much greater efficiency than it does now is very important. Thus , it is believed that novel light-trapping structures may help address this limitation and allow the cells to achieve much greater efficiency. Thus, in this thesis, such a novel, light-trapping method is proposed in Chapter 4.

1.3 Dispersion modeling and time domain simulation

Among the various of optical simulation tools, the finite-difference time-domain (FDTD) method [8, 9], due to its accuracy, robustness, and matrix-free calculations, has been a powerful technique for simulating wave propagation in dispersive media, such as magnetic media [10, 11], polymers [12], nanostructures [13, 14], and metamaterials [15]. In this thesis, the FDTD method was utilized to investigate the optical design of TFSCs.

Recently, many researchers have been attempting to simulate novel photovoltaic materials presented the light-trapping structures they have proposed. However, none of them suggested a simulation result that included wide frequency response, because a proper dispersion model has yet to be developed for certain materials. Two dispersion models have been reported, and they represent the dispersion characteristics of a-Si very well. The first one was the Tauc-Lorentz (TL) model, which is a combination of the Tauc model and the Lorentz model. Fig. 1.5 shows that this model represents the relative permittivity of a-Si very well. However, the model uses a very complicate form of ϵ_1, as shown in eq. 1.1.

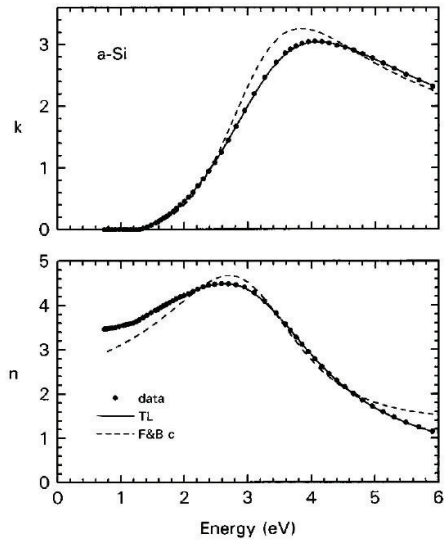

Fig. 1.5. Real and imaginary part of refractive index of amorphous silicon using Tauc-Lorentz model [16]

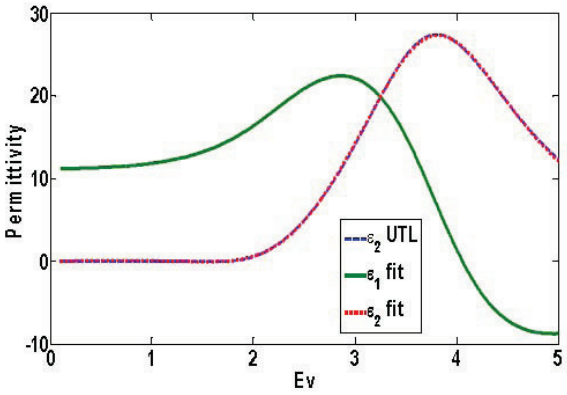

Fig. 1.6. Reltive permittivity of amorphous silicon using Double-Lorentz model [17]

$$\varepsilon_{1TL}(E) = \varepsilon_{1TL}(\infty) + \frac{1}{2}\frac{A}{\pi}\frac{C}{\zeta^4}\frac{a_{in}}{\alpha E_0} ln[\frac{(E_0^2 + E_g^2 + \alpha E_g)}{(E_0^2 + E_g^2 - \alpha E_g)}]$$
$$- \frac{Aa_{atan}}{\pi\zeta^4 E_0}[\pi - atan(\frac{2E_g + \alpha}{C}) + atan(\frac{-2E_g + \alpha}{C})] + 2\frac{AE_0C}{\pi\zeta^4}[E_g(E^2 - \gamma^2)$$
$$[\pi + 2atan(\frac{\gamma^2 - E_g^2}{\alpha C})]] - 2\frac{aE_0C}{\pi\zeta^4}\frac{E^2 + E_g^2}{E} ln(\frac{E - E_g}{E + E_g})$$
$$+ 2\frac{AE_0C}{\pi\zeta^4} E_g ln[\frac{|E - Eg|(E + E_g)}{\sqrt{E_0^2 - E_g^2)^2 + E_g^2 C^2}}]. \tag{1.1}$$

Even though the TL model represents the dispersion of a-Si very well, it is not applicable to time-domain simulation due to its extremely complicated form of ϵ_1.

Another research group suggested a new dispersion model for a-Si, which is called the two-pole Lorentz model [17]. Fig. 1.6 shows that this model, represents the relative permittivity of a-Si very well, but, as mentioned in [17], one of the two Lorentz poles has a negative value, and this eventually causes instability in 2-D and 3-D simulations.

As discussed in this section, most time-domain simulations have been conducted with single-frequency or narrowed-frequency systems [18, 19]. In Chapter 2 of this thesis, a new dispersion model is proposed for novel photovoltaic materials. Chapter 3 demonstrates the FDTD implementation of the proposed dispersion model with 1-D, 2-D and 3-D dispersive FDTD simulations. They are validated by comparison to

analytical solutions. Chapter 4 applies the proposed model to a novel and physically realistic light-trapping structure, using the statistically-correlated, random surface-texturing method. In Chapter 5, a new, solar-cell design is proposed in the sub-wavelength regime with the multi-variable optimization method. Finally, Chapter 6 summerizes the results of this thesis and suggests several follow up problems that are new and worthy of further investigation.

2. DISPERSIVE MODELING OF NOVEL PHOTOVOLTAIC MATERIALS

In the time domain simulation, it is very important to know the approaches that allow the FDTD method to model dielectric property like linear dispersion, nonlinearity nonlinear dispersion, and gain [8].

For many types of dispersive media, several modeling methods have been proposed such as Debye, Lorentz and Drude models [8, 20]. However, those models are insufficient for dispersive modeling of some novel photovoltaic materials such as amorphous silicon, CIGS, CZTS etc, because in the semiconductor materials, both the conducting term and non-conducting term must be taken into account in their wave equation. The wave equation considering both terms is a rather complicated and the solutions are somewhat difficult to interpret [21]. Nevertheless, a qualitative description of many of the optical properties of semiconductors is furnished by classical theory. As a result, there is promising modeling method called Tauc-Lorentz model [16] which shows very good agreement with measurement data of amorphous silicon. However, the Tauc-Lorentz model has exponential term in its equation and it eventually makes the FDTD implementation very difficult [22].

Recently, a quadratic complex rational function (QCRF) model was suggested for FDTD dispersive modeling for biological tissues [26, 27] in the frequency range from 400 MHz to 3 GHz [25]. It was shown that QCRF is simple and accurate, and thus suitable for dispersive media. Moreover, this dispersion model does not need an initial guess, different from extended Debye models. In this paper, the QCRF model will be applied to novel photovoltaic material with improved accuracy and stability using Particle Swarm Optimization(PSO). Toward this end, I introduce a weighting function to a QCRF matrix-solving equation and then apply a particle swarm optimization (PSO) [28] to attain accurate coefficients of QCRF. Note that the PSO is simple and

easy to determine the optimal solution in multi-domain problems for a wide range of applications. Eventually, the proposed QCRF/PSO method can yield an accurate polynomial function of complex permittivity along the measured data. Numerical examples are used to illustrate the validity of the proposed QCRF/PSO method at the next chapter.

2.1 QCRF model

Assume that there is discrete data representing the relative permittivity of a dispersive medium and it is expressed by

$$\varepsilon_{r,DATA}(\omega) = \varepsilon'(\omega) + j\varepsilon''(\omega) \tag{2.1}$$

where ε' and ε'' indicate the real part and the imaginary part of the relative complex permittivity of the dispersive material, respectively. They are usually obtained by measurement data or empirical models. The main goal for this work is to find a simple and accurate FDTD modeling for dispersive media. In this section, I employ a complex rational function model to represent the frequency responses of the dispersive medium. Although the proposed method can be expended to higher-order (cubic, quartic, etc) polynomials, it is constrained to a 2nd-order (quadratic) polynomial in this thesis, because the form of quadratic polynomial consumes the least amount of memory when it is applied to FDTD method and the higher order polynomial is also computationally inefficient. [25] The general form of the 2nd-order polynomial function, i.e., QCRF, is represented by

$$\varepsilon_{r,QCRF}(\omega) = \frac{N(\omega)}{D(\omega)} = \frac{A_0 + A_1(j\omega) + A_2(j\omega)^2}{1 + B_1(j\omega) + B_2(j\omega)^2}. \tag{2.2}$$

2.1.1 Formulation

Before proceeding with the development of QCRF/PSO model, it is worthwhile to briefly describe the analytic procedure of QCRF model [25]. By comparing QCRF with measurement data, the error is given by $e(\omega) = \varepsilon_{r,DATA}(\omega) - \varepsilon_{r,QCRF}(\omega)$. From

the complex-curve fitting technique suggested in [31,32] we multiply $e(\omega)$ by $D(\omega)$ to analytically obtain coefficients of QCRF:

$$\begin{aligned} D(\omega)e(\omega) = &[(1-\omega^2 B_2)R(\omega) - \omega B_1 I(\omega) - A_0 + \omega^2 A_2] \\ &+ j[\omega B_1 R(\omega) + (1-\omega^2 B_2)I(\omega) - \omega A_1]. \end{aligned} \tag{2.3}$$

Now, the function E representing a *relative* error is defined by

$$\begin{aligned} E &= \sum_{k=1}^{M} |D(\omega_k)e(\omega_k)|^2 \\ &= \sum_{k=1}^{M} [(1-\omega_k^2 B_2)R(\omega_k) - \omega_k B_1 I(\omega_k) - A_0 + \omega_k^2 A_2]^2 \\ &+ [\omega_k B_1 R(\omega_k) + (1-\omega_k^2 B_2)I(\omega_k) - \omega_k A_1]^2 \end{aligned} \tag{2.4}$$

where ω_k and M represent the sampling frequency and the maximum sampling index, respectively. To find the minimum relative error, the E function is differentiated with respect to each of QCRF coefficients, i.e., $\frac{\partial E}{\partial A_0} = 0$, $\frac{\partial E}{\partial A_1} = 0$, $\frac{\partial E}{\partial A_2} = 0$, $\frac{\partial E}{\partial B_1} = 0$, and $\frac{\partial E}{\partial B_2} = 0$. After arranging five simultaneous equations, it becomes the following matrix equation:

$$\begin{bmatrix} \lambda_0 & 0 & -\lambda_2 & T_1 & S_2 \\ 0 & \lambda_2 & 0 & -S_2 & T_3 \\ \lambda_2 & 0 & -\lambda_4 & T_3 & S_4 \\ T_1 & -S_2 & -T_3 & U_2 & 0 \\ S_2 & T_3 & -S_4 & 0 & U_4 \end{bmatrix} \begin{bmatrix} A_0 \\ A_1 \\ A_2 \\ B_1 \\ B_2 \end{bmatrix} = \begin{bmatrix} S_0 \\ T_1 \\ S_2 \\ 0 \\ U_2 \end{bmatrix} \tag{2.5}$$

where

$$\begin{aligned} \lambda_h &= \sum_{k=1}^{M} \omega_k^h \\ S_h &= \sum_{k=1}^{M} \omega_k^h R(\omega_k) \\ T_h &= \sum_{k=1}^{M} \omega_k^h I(\omega_k) \\ U_h &= \sum_{k=1}^{M} \omega_k^h [R^2(\omega_k) + I^2(\omega_k)] \end{aligned} \tag{2.6}$$

Finally, the unknown QCRF coefficients are simply determined by solving this 5×5 matrix equation. Note that the work that minimizing the *relative* error leads to reduce the *real* error, since the former is nearly proportional to the latter, as mentioned in [32]. However, it should be emphasized that the roots, found by this method, will not be the optimum value, due to the fact that the this analytic method defines the relative error as real error multiplied by denominator of QCRF equation. As it will be discussed in the PSO/QCRF section, the conventional QCRF method has limitation when the dispersive material has sharp variation in its relative permittivity. Also, the analytic result obtained by the conventional QCRF method sometimes shows slightly negative value on its ε'' when the measurement data for ε'' is very close to zero. The optimization method minimizing the real error will be discussed in the PSO/QCRF section.

2.1.2 Stability

It should be mentioned that the QCRF dispersion model has its own condition satisfying Kramers-Kronig relation. As explained in [8], the pole of the (2.2) should be located in the upper half plane of real and imaginary axis [8]. The pole of (2.2) is simply obtained by the formula for the roots of quadratic polynomial as follow

$$\omega_p^{\pm} = \frac{-B_1 \pm \sqrt[2]{B_1^2 - 4B_2}}{2B_2}. \tag{2.7}$$

In fact, the most of curves obtained by QCRF method have positive (B_1, B_2) except for the gain media. The materials, which have negative coefficients for (B_1, B_2) in the QCRF method, will be explained at QCRF/PSO section. It should be mentioned that there is another stability issue called 'numerical stability' which we also have to consider about. The numerical stability issue is tested in the chapter 3 and eventually it suggested to us that setting all five QCRF coefficients positive allows us to avoid numerical stability issue in FDTD simulation.

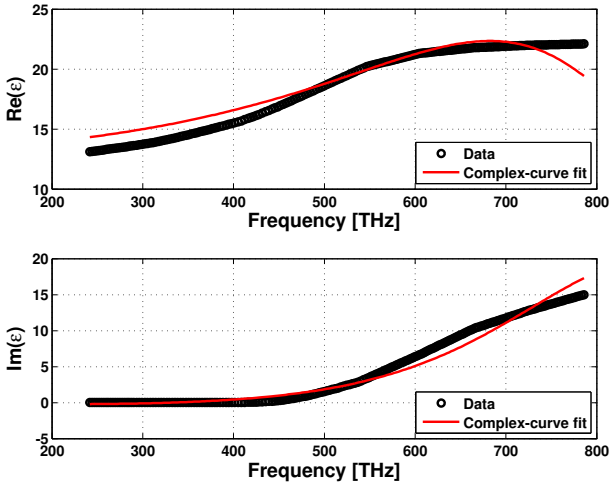

Fig. 2.1. Relative permittivity of a-Si. The solid lines and symbols indicates the QCRF model and a-Si measurement data respectively.

2.1.3 Complex curve fitting

Crystalline silicon(c-Si) has been a dominant material in solar cell industry for many years. However, because of certain drawbacks found in silicon solar cells which include indirect bandgap, weaker absorption and higher Auger-recombination, now many researchers are looking at the another promising candidate material which can substitute c-Si. Amorphous silicon(a-Si), CdTe, CIGS, GaAs are chosen in this work and their dispersive characteristic is modeled by proposed method. Also, the the relative permittivity of silver and silicon substrate which are considered as dispersive materials in solar cell structure, modeled by this method. The measurement data for the novel photovoltaic materials are extracted from the following references [33,34](a-Si), [35](CdTe), [36](CIGS), [35](GaAs), [37](Si substrate), [36](silver).

As shown in Fig. 2.1, the QCRF model fits fairly well with measurement data. The quantified root mean square error is 3.763(%) for a-Si curve fitting. This curve fitting might be considered as large deviation from the initial measurement data, so, it should be emphasized that the complex curve fitting for a-Si is one of the most difficult work among the various dispersive modelings, because the imaginary

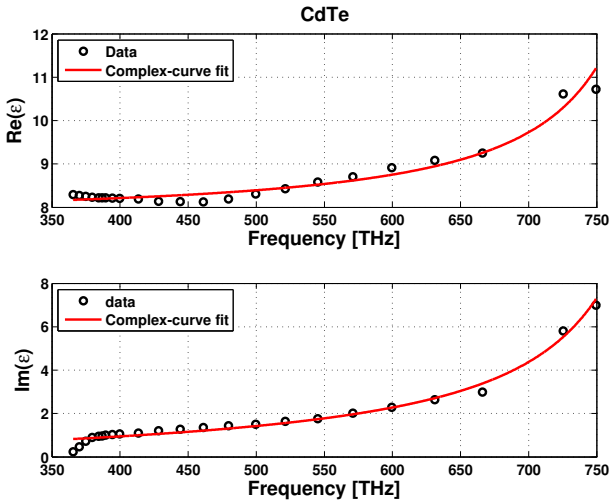

Fig. 2.2. Relative permittivity of CdTe. The solid lines and symbols indicates the QCRF model and CdTe measurement data respectively. Corresponding QCRF coefficients are given in Table. 2.1

part of epsilon is varying very sharply between relatively wide frequency range. For example, the imaginary part of epsilon at the frequency of 242THz and 786THz are 0.002857194 and 14.99634269, respectively. The relative variation between those two frequencies is around fifty thousand. On the other hand, the relative variation for common dispersive material (e.g concrete, human tissue, etc) [25, 38] is much less than a-Si at the frequency range that we are interested in.

As shown in Fig. 2.2 - 2.5 and Table. 2.1, the QCRF model application for the novel photovoltaic materials seems very promising except the fact that stability of this application has not been tested. Also, in Fig. 2.1, the imaginary part of relative permittivity of QCRF curve fitting shows slightly less than zero. Although the quantified error caused by imaginary part of epsilon might be very trivial, negative value of imaginary part of relative permittivity can potentially cause unexpected physical effect like electric field gain in FDTD simulation. In Table. 2.1, the QCRF coefficients for silver and CdTe have negative numbers in (B_1, B_2). As mentioned in the previous section, negative numbers in (B_1, B_2) can cause stability issue.

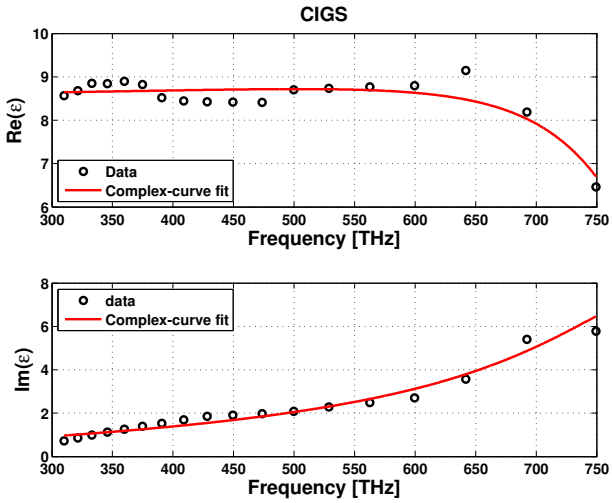

Fig. 2.3. Relative permittivity of CIGS. The solid lines and symbols indicates the QCRF model and CIGS measurement data respectively. Corresponding QCRF coefficients are given in Table. 2.1

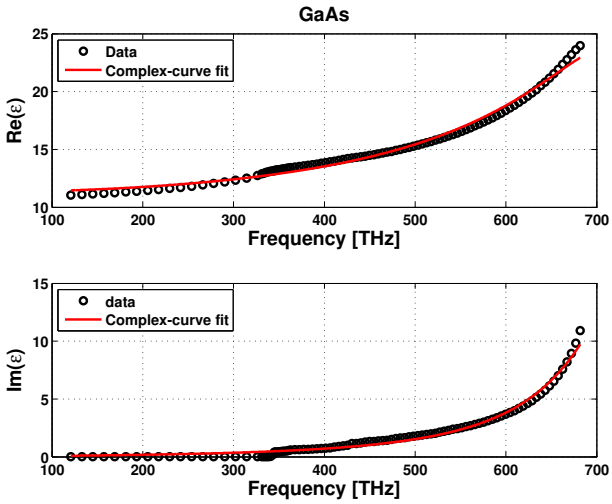

Fig. 2.4. Relative permittivity of GaAs. The solid lines and symbols indicates the QCRF model and GaAs measurement data respectively. Corresponding QCRF coefficients are given in Table. 2.1

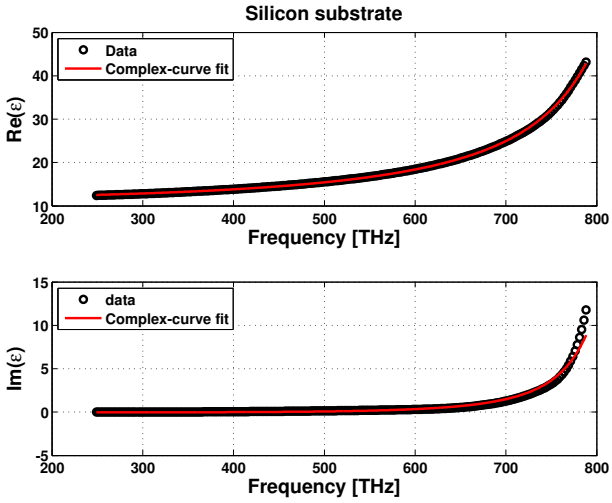

Fig. 2.5. Relative permittivity of silicon substrate. The solid lines and symbols indicates the QCRF model and silicon substrate measurement data respectively. Corresponding QCRF coefficients are given in Table. 2.1

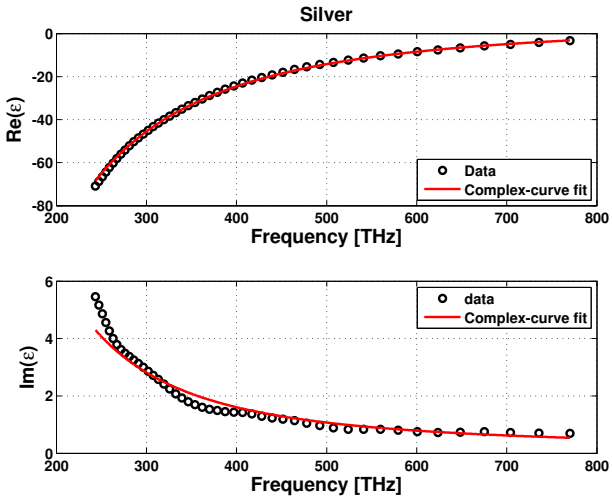

Fig. 2.6. Relative permittivity of silver. The solid lines and symbols indicates the QCRF model and silver measurement data respectively. Corresponding QCRF coefficients are given in Table. 2.1

In order to solve stability issue and negative value of imaginary part of relative permittivity, the optimization technique will be applied at following section. Also, ass mentioned in section 2.1.1 the optimization technique that minimizing the real error will be discussed at the next section.

2.2 PSO/QCRF model

Despite simplicity and accuracy of the previous analytic approach, the conventional QCRF model cannot always be fitted to measurement data, especially when they vary rapidly over the frequency of interest as shown in Fig. 2.1 [25]. This is because the analytic approach does not consider the frequency range in which the most errors occur. In other words, it does not emphasize the places where significant variations occur. Also, the negative QCRF coefficients as shown in Table. 2.1 potentially cause stability issue when it is tested in the FDTD simulation [25]. In order to solve these problems, the constrained Particle Swarm Optimization(PSO) method is applied finding the coefficients of the conventional QCRF method. Separate solutions will be suggested for two different issues.

Table 2.1
QCRF Coefficients and Error for novel photovoltaic materials

	a-Si	CdTe	CIGS	GaAs	Si substrate	silver
A_0	11.180	8.020	8.587	11.073	11.901	-558.192
A_1	2.305×10^{-15}	-3.048×10^{-16}	-6.342×10^{-17}	5.377×10^{-16}	1.509×10^{-16}	-6.855×10^{-15}
A_2	-2.867×10^{-31}	2.731×10^{-31}	2.510×10^{-31}	1.011×10^{-31}	1.614×10^{-31}	-1.460×10^{-29}
B_1	1.516×10^{-16}	-2.098×10^{-18}	4.285×10^{-17}	5.422×10^{-17}	1.079×10^{-17}	-2.137×10^{-16}
B_2	3.017×10^{-32}	3.693×10^{-32}	3.361×10^{-32}	3.749×10^{-32}	3.366×10^{-32}	-2.842×10^{-30}
E	3.763(%)	1.602(%)	2.915(%)	3.129(%)	1.784(%)	2.221(%)

2.2.1 Improvement of accuracy

One possible approach to tackle the first problem, rapidly changing data, is to use more sampling data in the frequency range where more errors occur [25] than to use evenly-spaced sampling data. However, this approach is somewhat ambiguous and user-dependent. To improve the accuracy of QCRF in a systematic way, in this work, I consider a weighting function in (2.4). The weighting function is defined as $\zeta(\omega_k)$ which is a discrete function whose domain is the number of maximum sampling index M. Consequently, (2.4) is modified as

$$E = \sum_{k=1}^{M} |D(\omega_k)e(\omega_k)|^2 \zeta(\omega_k). \tag{2.8}$$

With some manipulations, the 5×5 matrix equation is obtained same as (2.5) with the modified matrix components as follows

$$\begin{aligned} \lambda_h &= \sum_{k=1}^{M} \omega_k^h \zeta(\omega_k) \\ S_h &= \sum_{k=1}^{M} \omega_k^h R(\omega_k)\zeta(\omega_k) \\ T_h &= \sum_{k=1}^{M} \omega_k^h I(\omega_k)\zeta(\omega_k) \\ U_h &= \sum_{k=1}^{M} \omega_k^h [R^2(\omega_k) + I^2(\omega_k)]\zeta(\omega_k). \end{aligned} \tag{2.9}$$

Now, proper $\zeta(\omega_k)$ should be found in order to enhance the accuracy of QCRF curve fitting along the measurement data. Toward this purpose, the PSO algorithm is applied here. In the PSO algorithm [28], the particles (initially located in random position) "visit" to the weighted QCRF curve-fitting function and return with carrying the fitness evaluated by the inverse of the *real* root mean square ($r.m.s$) error as follows

$$\begin{aligned} E_{r.m.s} &= \sqrt{\frac{\sum_{k=1}^{M} |\varepsilon_{r,DATA}(\omega_k) - \varepsilon_{r,QCRF}(\omega_k)|^2}{\sum_{k=1}^{M} |\varepsilon_{r,DATA}(\omega_k)|^2}} \\ &= \frac{1}{fitness}. \end{aligned} \tag{2.10}$$

Then the fitness of each particle is compared with its previous best fitness carried by itself ($pBest$) and the previous best fitness carried by entire particles ($gBest$). Through these comparisons, the next position of each particle is determined as the following equation [28]:

$$\begin{aligned} v_n^{i+1} = \nu \cdot v_n^i + c_1 \cdot rand() \cdot (pBest_n^i - x_n^i) \\ + c_2 \cdot rand() \cdot (gBest_n^i - x_n^i) \end{aligned} \tag{2.11}$$

where v_n^{i+1} is the velocity of $i+1$-th iteration in the n-th dimension, ν is a weighting of previous velocity, x_n^i is the current position of i-th iteration in the n-th dimension, and $rand()$ is a function generating a random number between from 0 to 1. Note that c_1 and c_2 are the cognitive parameter and the social parameter respectively and these parameters determine the tendency of particles that pursuing the local best position (c_1) or the global best position (c_2) [28].

Many researchers working on PSO suggested the standard initial parameter setting as $c_1 = c_2 = 2$, $\nu = 1$ and the number of particle $N = 30$ [28–30]. The optimum initial parameters of PSO algorithm are different for each application. Properly chosen parameters may increase the probability of converging to the true solution and also may lead to converge slightly faster. In this work, I add run-concept to the original PSO algorithm rather than researching on optimum initial parameters for each application. In other words, the QCRF/PSO generates a number of sub-solutions corresponding to the number of runs. And then the best solution is sorted among them. In this QCRF/PSO simulation, as will be performed by next section, the 50 runs has been performed for each application. The entire algorithm used in this proposed simulation is shown in Fig. 2.7. As alluded to previously, the PSO algorithm contributes to the improvement in the accuracy of the QCRF dispersion model. It is worthwhile to note that the QCRF/PSO algorithm is performed only once before FDTD time marching and thus the computational costs of updating electromagnetic fields in the resulting FDTD is not increased.

One may try to apply the PSO algorithm to determine the QCRF coefficients directly, rather than determine the weighting function of QCRF (as in this approach).

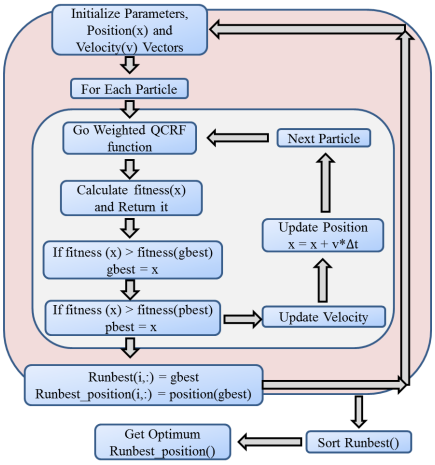

Fig. 2.7. Flowchart of QCRF/PSO method.

However, as explained in the paper [31], this trial will not success since the solution space is too large to be determined only by the PSO algorithm. It is usually formed in the range of more than 20 orders of magnitude for many types of dispersive media.

2.2.2 Solving stability issues

The PSO method also can be applied to enforce the QCRF coefficients as positive. It can be simply achieved by adding following statement

$$\begin{aligned} &if((B1 < 0) or (B2 < 0)) \\ &fitness = fitness + \alpha \end{aligned} \tag{2.12}$$

, where α is the enforcing factor. This factor modifies the fitness of each particle, obtained by QCRF curve fitting, when the QCRF coefficients are less than zero. The enforcing factor should be relatively larger than the usual fitness of the QCRF curve fitting, because the PSO algorithm will ignore the relatively small amount of error added by eq. 2.12, when α is relatively smaller than the fitness. In this problem, the enforcing factor is set to 100 which is more than 15 times greater than the common fitness. The fitness means R.M.S error calculated at the QCRF curve fitting in this problem. The rest of algorithm is same as described in previous section.

certain photovoltaic materials like a-Si show sharply converging shape in their relative permittivity curves. When the relative permittivity curve converges to zero, it is important to check that the dispersive modeling method does have negative value in its imaginary part of relative permittiviy. The negative value in it can be thought as gain medium which is not intended in a photovoltaic system. As shown in Fig. 2.1, there is negative value at the low frequency range around 300THz. Even though the amount of error caused by this negative value does not affect to the total error significantly, the FDTD simulation result using Fig. 2.1 generates unintended physical effect(gain media)). In order to solve this issue, another statement is added in the PSO/QCRF method.

$$\begin{aligned} &if(Im(\epsilon) < 0) \\ &fitness = fitness + \alpha, \end{aligned} \tag{2.13}$$

where α is the enforcing factor as described in the eq. 2.12. As mentioned before, the enforcing factor is set to 100 which is much greater than the common fitness value obtained by R.M.S error calculation.

2.2.3 PSO/QCRF curve fitting

By applying proposed PSO/QCRF algorithm, new curve fitting for the dispersive material is obtained. This PSO/QCRF curve fitting has advantages over the conventional QCRF curve fitting as mentioned in the previous section. To show the advantage of it, two samples are selected among the 6 novel photovoltaic materials mentioned in the previous section. The first sample is silver which shows negative QCRF coefficients and 2.221(%) R.M.S error in its conventional QCRF curve fitting. The second sample is amorphous silicon which shows negative QCRF coefficient, negative value on its imaginary part of relative permittivity and 3.763(%) R.M.S error. It should be emphasized that another novel photovoltaic materials can be applied to the proposed PSO/QCRF algorithm, but I focused on these two materials, in order to show the proposed algorithm works properly.

As shown in Table. 2.2, the proposed method enhanced the accuracy of dispersive modeling for silver and it also successfully enforced its coefficients as positive values. The R.M.S error reduced from 2.221(%) to 0.663(%). The PSO/QCRF curve fitting, as shown in Fig. 2.8, matches better than the curve fitting shown in Fig. 2.6. However, the error of amorphous silicon sample is increased when it is applied to PSO/QCRF method. The main reason is that the PSO/QCRF algorithm ensures that the QCRF coefficients are positive as well as the imaginary part of relative permittivity. It sacrifices slight amount of fidelity in order to satisfy the important physical constraints. Even though the accuracy decreased slightly as shown in Fig. 2.9, it still represents

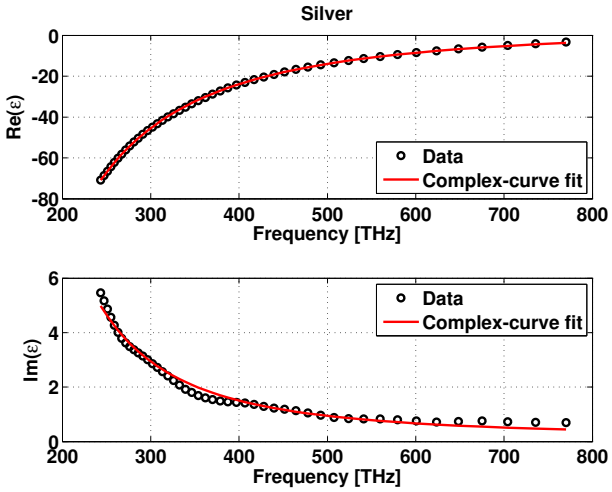

Fig. 2.8. Relative permittivity of silver. The solid lines and symbols indicates the PSO/QCRF model and silver measurement data respectively. Corresponding QCRF coefficients are given in Table. 2.2

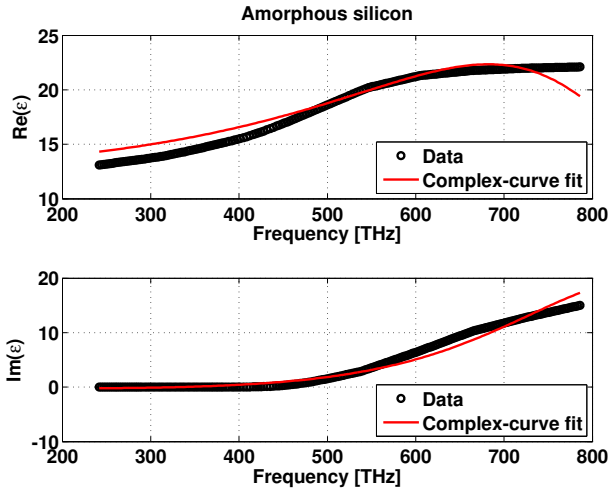

Fig. 2.9. Relative permittivity of amorphous silicon. The solid lines and symbols indicates the PSO/QCRF model and amorphous silicon measurement data respectively. Corresponding QCRF coefficients are given in Table. 2.2

the physical property of amorphous silicon fairly well. Especially, the exponential increase of the imaginary part of relative permittivity around the frequency of 400THz is successfully modeled by proposed method with attaining stability as well. The accuracy of the proposed modeling method will be tested in the next chapter.

Table 2.2
PSO/QCRF Coefficients and Error for novel photovoltaic materials

	a-Si	CdTe	CIGS	GaAs	Si substrate	silver
A_0	13.203	8.020	8.587	11.073	11.901	7.431×10^{5}
A_1	1.758×10^{-15}	-3.048×10^{-16}	-6.342×10^{-17}	5.377×10^{-16}	1.509×10^{-16}	7.744×10^{-12}
A_2	3.846×10^{-32}	2.731×10^{-31}	2.510×10^{-31}	1.011×10^{-31}	1.614×10^{-31}	1.598×10^{-26}
B_1	1.140×10^{-16}	-2.098×10^{-18}	4.285×10^{-17}	5.422×10^{-17}	1.079×10^{-17}	3.462×10^{-13}
B_2	3.568×10^{-32}	3.693×10^{-32}	3.361×10^{-32}	3.749×10^{-32}	3.366×10^{-32}	4.236×10^{-27}
E	6.550(%)	1.602(%)	2.915(%)	3.129(%)	1.784(%)	0.663(%)

3. TIME DOMAIN SIMULATION : A-SI

In this chapter, the proposed dispersive FDTD simulation with a QCRF model will be validated against theory and also against non-dispersive FDTD. FDTD implementation of the QCRF dispersion model is first discussed prior to showing the simulation results. Then, in the 1-D space, the proposed QCRF dispersive FDTD simulation results will be compared with theory which is called Snell's law. After the 1-D simulation results are confirmed against theoretical calculation, 2-D and 3-D QCRF dispersive FDTD simulation results will be compared with a non-dispersive FDTD simulation. The procedure of comparing the dispersive FDTD with non-dispersive FDTD ensures the accuracy of the proposed dispersive FDTD method and its ability to model and simulate the novel photovoltaic materials listed in Chapter 2.

3.1 FDTD implementation of QCRF dispersion model

FDTD update equations for the QCRF model can be easily obtained by the standard difference scheme. For example, applying the standard difference scheme to the temporal derivatives in the constitutive relation results in, the final update equation for $\vec{E}^{n+1}$ as follows [25]

$$\vec{E}^{n+1} = C_a\vec{E}^{n} + C_b\vec{E}^{n-1} + C_c\vec{D}^{n+1} + C_d\vec{D}^{n} + C_e\vec{D}^{n-1} \tag{3.1}$$

$$
\begin{aligned}
C_a &= -2(\alpha_0 - \alpha_2)/(\alpha_1 + \alpha_2) \\
C_b &= (\alpha_1 - \alpha_2)/(\alpha_1 + \alpha_2) \\
C_c &= (\beta_1 + \beta_2)/(\alpha_1 + \alpha_2) \\
C_d &= 2(\beta_0 - \beta_2)(\alpha_1 + \alpha_2) \\
C_e &= -(\beta_1 - \beta_2)/(\alpha_1 + \alpha_2)
\end{aligned}
\tag{3.2}
$$

$$
\begin{aligned}
\alpha_0 &= A_0 \Delta t^2 \\
\alpha_1 &= A_1 \Delta t \\
\alpha_2 &= 2A_2 \\
\beta_0 &= \Delta t^2/\varepsilon_0 \\
\beta_1 &= B_1 \Delta t/\varepsilon_0 \\
\beta_2 &= 2B_2/\varepsilon_0
\end{aligned}
\tag{3.3}
$$

The update equations for $\vec{D}^{n+1}$ and $\vec{H}^{n+1/2}$ can be simply obtained by applying the standard difference scheme to the spatial derivatives in Maxwell's curl equations. Also, by employing complex stretching variables in spatial derivatives, one can straightforwardly implement perfectly matched layer (PML) boundary conditions [39–42].

3.2 1D FDTD simulation against theory

First, the accuracy of QCRF-based dispersive FDTD was verified against theory. In a 1-D simulation, an uniform plane wave is incident from air to the QCRF material region at z=0 as shown in Fig 3.1. In this work, the QCRF material was selected only as a-Si/QCRF model, because simulating every material listed in the last chapter would not be meaningful since the QCRF model just requires users to put different QCRF coefficients for different materials. Anything except for the five QCRF coefficients is the same when the QCRF model is applied to other materials.

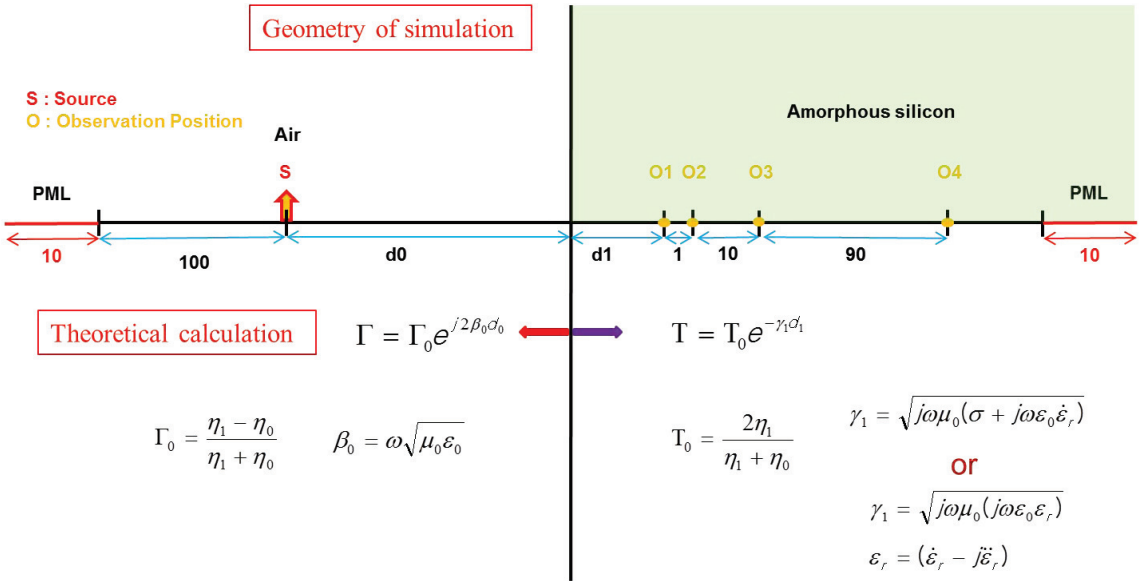

Fig. 3.1. Geometry setting for 1-D FDTD simulation and theoretical calculation. d0 and d1 will be noted for each simulation result.

The simulation domain is constructed with an entire set of 202 cells which include 110 cells of the QCRF material region, 110 cells of the air region and 10 cells of the PML region overlapped with air and the QCRF material as shown in Fig 3.1. The source point is located at the 110th cell.

As shown in Fig. 3.2, the FDTD simulation was performed twice, first at the free-space and second at the QCRF materials as shown in Fig. 3.1. The simulation results obtained from free-space simulation were applied when we calculated the reflection coefficient and the transmission coefficient. Basically, in order to calculate the amount of wave reflected from the material boundary, I subtracted the intensity of the wave obtained by dispersive simulation from the intensity of incident wave obtained by free-space simulation. In other words, the blue dotted line was subtracted by the red solid line as shown in Fig. 3.2.

The intensity of the transmitted wave was measured at the observation point denoted as 'O1' as shown in Fig. 3.1. As described in the [43], the reflection coefficient and transmission coefficient are defined as

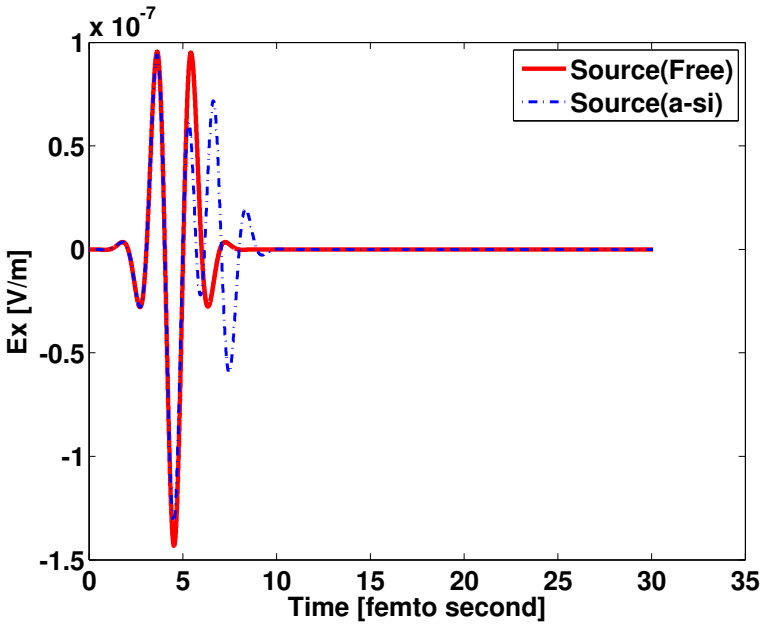

Fig. 3.2. 1D FDTD results in time domain with two different geometry settings. The red curve indicates simulation in the freespace and the blue dotted line indicates simulation with QCRF material.

$$\Gamma = E_{ref}/E_{inc}, \tag{3.4}$$

$$\tau = E_{tran}/E_{inc}, \tag{3.5}$$

where E_{ref}, E_{inc} and E_{trans} are the intensity of the reflected electric field, incident electric field and transmitted electric field respectively. As mentioned previously, the intensity of the reflected wave is defined as

$$E_{ref} = E_{dispersive} - E_{freespace}. \tag{3.6}$$

Where $E_{dispersive}$ is the intensity of the electric field at the dispersive FDTD simulation and $E_{freespace}$ is the intensity of the electric field at the free-space simulation. The propagation constant β and the attenuation constant α are also calculated with measurement data and eventually they are compared to those of the simulation results. The equations used in calculation β and α are described in Fig. 3.1. In this simulation, I limited the distance(d1) between observation point 1 and the material boundary as one cell, in order to prevent the attenuation constant that dominates entire wave propagating equation. In the FDTD simulation, the distance(d1) between the material boundary and observation point 1 is also selected to be the same as the theoretical calculation, so there is no error from mismatched geometry.

The frequency domain data was obtained by performing a Discrete Time Fourier Transform(DTFT). The DTFT procedure basically follows by the eq. 3.7

$$X(\omega) = \Sigma_{n=0}^{\infty} x[n] e^{-iwn} \tag{3.7}$$

where ω is limited in the frequency range that we are interested in. As shown in Fig. 3.3, the time domain simulation results are converted to frequency domain. The

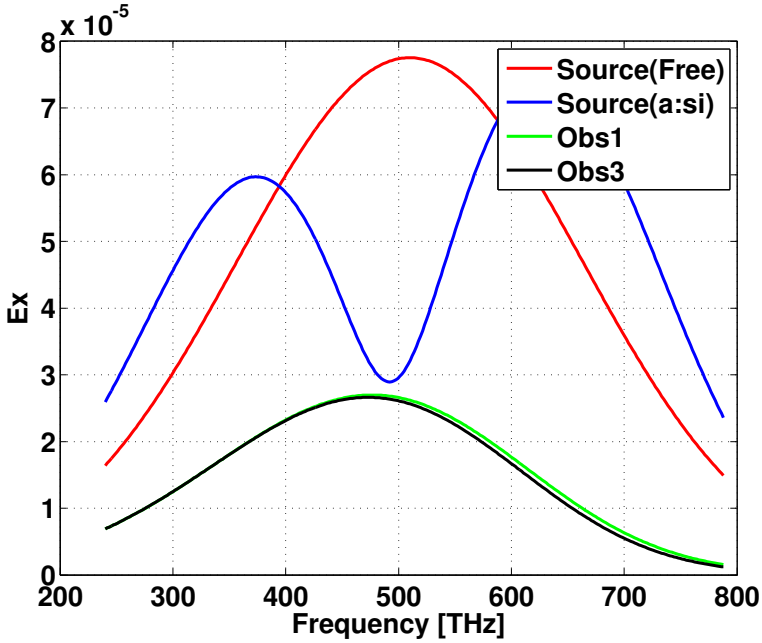

Fig. 3.3. 1D FDTD result in the frequency domain. The red curve indicates the simulation result in freespace and the blue dotted line indicates the simulation with QCRF materials. 'Obs' means the observation point as explained in Fig. 3.1

frequency domain result shows that the intensity of the field is gradually decreasing when the frequency is increased. This means the active material(a-Si) has a better absorption at the higher frequency. Also, it is possible to check that observation point 4 shows the lowest intensity among the four observation points. This means the incident wave attenuates in the active material.

As shown in Fig. 3.4, the reflection coefficient and transmission coefficient, calculated with the dispersive FDTD simulation results, agree well with those of the theoretical approach. It should be mentioned the frequency range applied in this result was limited from 240THz to 780THz which is roughly from 385nm to 1250nm in terms of free-space wavelength, because the internal quantum efficiency(IQE) of most a-Si solar cell shows a meaningful value at this frequency range.

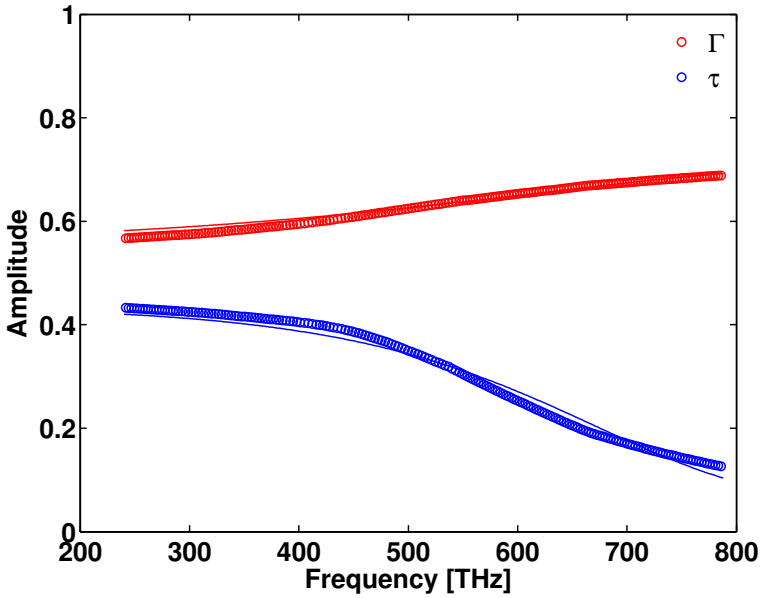

Fig. 3.4. The red dot represents the reflection coefficient which is analytically calculated. The red line represents the reflection coefficient calculated by FDTD simulation. The blue dot represents the transmission coefficient which is analytically calculated. The blue line represents the transmission coefficient calculated by FDTD simulation

In conclusion, the QCRF dispersion model was successfully implemented in the 1D FDTD scheme. In the 1D dielectric slab geometry, the simulation result and theoretical calculation result shows very good agreement as shown in Fig. 3.4.

3.3 2D

In the previous section, the accuracy of the proposed dispersive FDTD method was proven with the theoretical approach. In this section, QCRF-based dispersive FDTD is compared with non-dispersive FDTD in 2D geometry. As shown in Fig. 3.5, the simulation is performed on the 2-D space (120x60 cells) and a square-shaped QCRF/a-Si material (30x60 cells) is implemented at the center of the simulation region. The source point is located 30 cells away from the center of the QCRF/a-Si region. Also, the first observation point called 'absorption 1' is measured at the

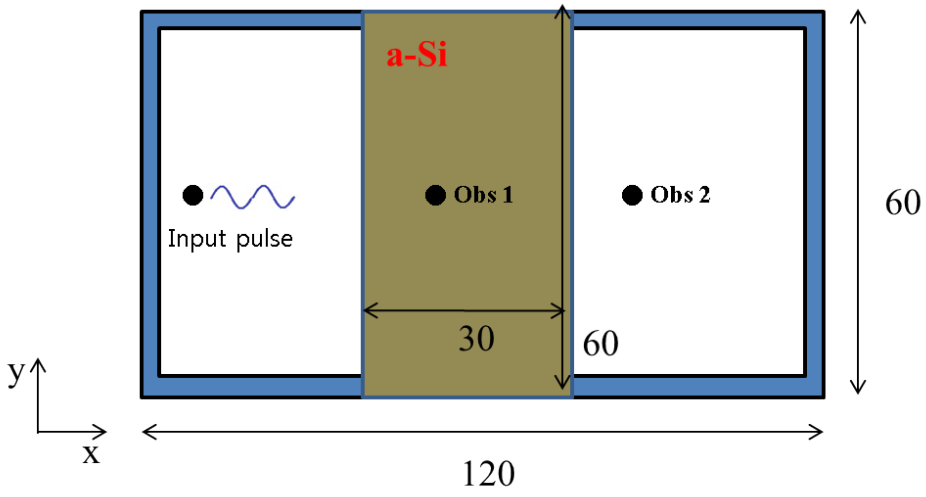

Fig. 3.5. Geometry setting for 2-D dispersive FDTD and non-disperisve FDTD simulation.

center of the QCRF/a-Si region and the second observation point called 'absorption 2' is measured at the outside of the QCRF/a-Si region, 30 cells away from the center of QCRF/a-Si region. In a non-dispersive FDTD simulation, a DC off-set sinewave is excited and many simulations are performed over the frequency of interests. For the non-dispersive FDTD simulation, the update equation is derived from the basic Maxwell equation [8].

The conventional FDTD update equations for lossy dielectrics [8] are applied to the non-dispersive FDTD simulation and the values of relative permittivity and conductivity are collected from the experimentally measured data [33]. The conventional FDTD update equation is

$$\nabla \times H = J + \frac{\partial D}{\partial t}. \tag{3.8}$$

The eq. 3.8 can be written in another form as eq. 3.9

$$\frac{\partial E}{\partial t} = \frac{1}{\varepsilon}[\nabla \times H + \sigma E] \tag{3.9}$$

$\frac{\partial E}{\partial t}$ can be divided in to $\frac{E^{n+1}-E^n}{\Delta t}$ by employing a standard finite difference scheme. Then Maxwell's curl equation can be written as a FDTD update equation in the form below:

$$E^{n+1} = E^n + \frac{\Delta t}{\varepsilon}[\nabla \times H + \frac{\sigma}{2}(E^{n+1} + E^n)]. \tag{3.10}$$

If it is limited in the E_x field component, the resulting equation is as below

$$E_x^{n+1} = C_{eax}E_x^n + C_{eax}(\frac{\Delta H_z}{\Delta y} - \frac{\Delta H_y}{\Delta z}), \tag{3.11}$$

where

$$C_{eax} = \frac{1-\sigma\Delta t/2\varepsilon}{1+\sigma\Delta t/2\varepsilon} \tag{3.12}$$

$$C_{bax} = \frac{2\Delta t}{2\varepsilon+\sigma\Delta t} \tag{3.13}$$

From eq. 3.9 eq. to 3.13, the constant dispersion model is investigated in order to make a comparison with the proposed QCRF dispersion model. I should also mentioned here that the constant dispersion model, derived in the above equations, is also used in the Chapter 4 and 5, because some important photovoltaic materials like SiO2 and ITO show an almost constant dispersion characteristic in the frequency range that we are interested in.

The update equation for the proposed QCRF dispersion FDTD is denoted in the FDTD implementation section. Note that, for a QCRF-based dispersive FDTD, a differential-Gaussian-modulated sinewave is used for wide-band excitation and thus the frequency response can be obtained by discrete Fourier transform.

As shown in Fig. 3.6, the intensity of the input pulse is attenuated in the QCRF material region so that the intensity of the electric field at observation point 1 is

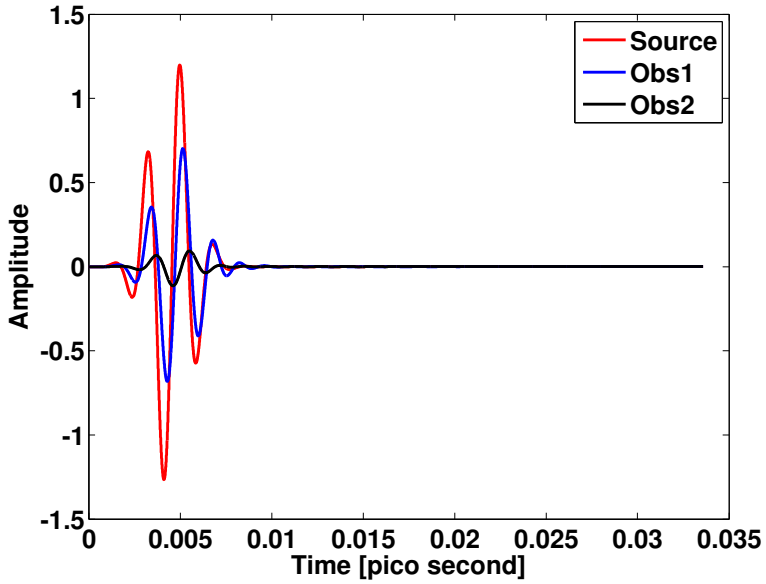

Fig. 3.6. 2D FDTD result in the time domain with a gaussian modulated sinewave. The red curve indicates the intensity of wave at the position that an input pulse is applied. The 'Obs' indicates an observation point as explained in Fig. 3.5.

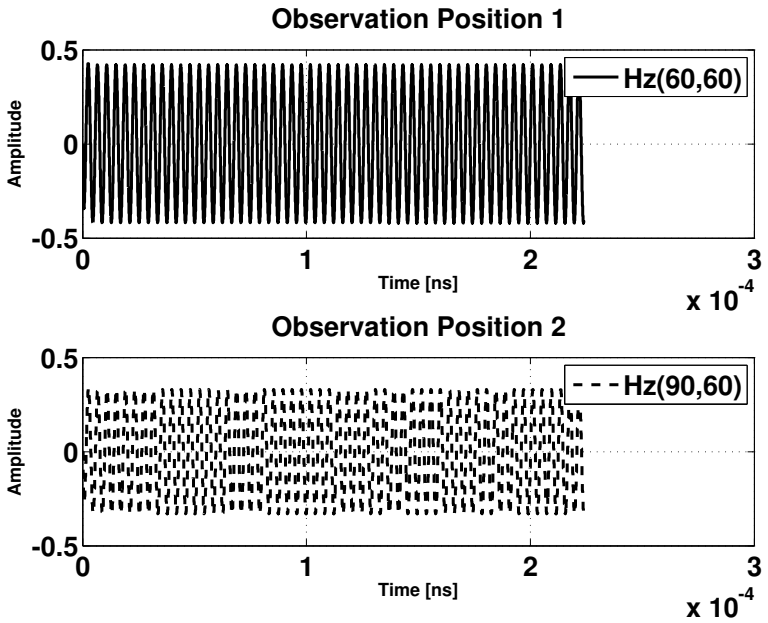

Fig. 3.7. 2D FDTD results in the time domain with a single frequency sinewave. The upper figure indicates the intensity of the wave observed at observation point 1 and the bottom figure indicates the intensity of the wave observed at observation point 2.

almost 50% less than the initial pulse. The field intensity measured at observation point 2 is much less than the field intensity measured at observation point 1, which means the wave is decayed further along the propagation and it is also reflected at the boundary of the QCRF material and air. As shown in Fig. 3.7, the single frequency simulation also shows that the intensity of the input pulse is decreased by almost 50% from observation point 1 to observation point 2. After the time domain simulation data is obtained, it is transformed to frequency domain data by applying DTFT. As shown in Fig. 3.8, the peak of the normalized input pulse in the frequency domain is set to 1 and the peaks of the pulse measured at observation point 1 and 2 should be relatively less than the intensity of the input pulse.

After transformed to frequency domain, the 'Absorption' term is defined like below:

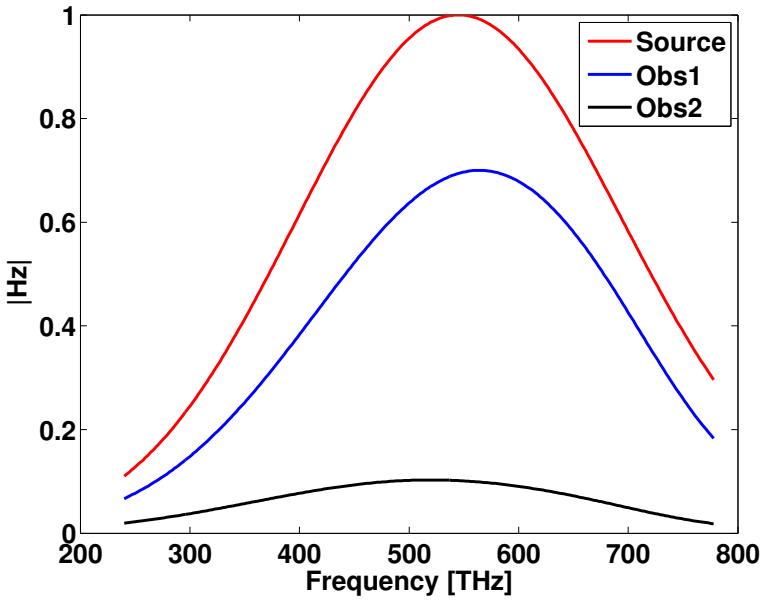

Fig. 3.8. 2D FDTD results in the frequency domain with gaussian modulated sinewave. The red curve indicates the intensity of wave at the position that input pulse is applied. The 'Obs' indicates an observation point as explained in Fig. 3.5.

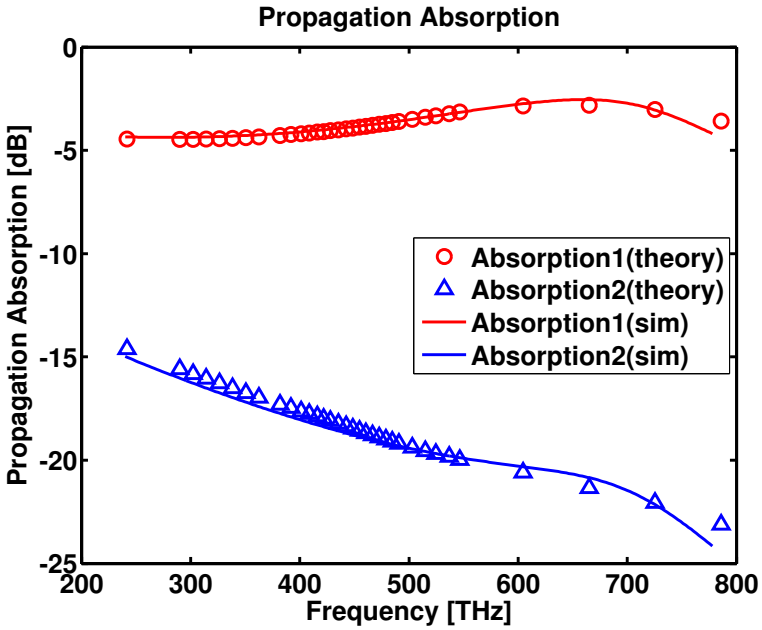

Fig. 3.9. Wave propagation absorption defined in eq. 3.14. The symbol indicates the absorption calculated from the single-frequency FDTD simulation and the line indicates the absorption calculated from the wide frequency FDTD simulation.

$$\text{Absorption} = 20 * \log[|H_{z,\text{material}}|/|H_{z,\text{free}}|] \tag{3.14}$$

where $H_{z,material}$ is the field intensity at the simulation with the proposed structure and $H_{z,free}$ is the field intensity at the free space simulation. As shown in Fig. 3.9, the single frequency simulation result, which is denoted as a symbol in the figure, matches very well with the QCRF dispersive FDTD simulation result which is denoted as a line. According to Fig. 3.9, amorphous silicon shows strong absorption over the frequency range from 240THz to 780THz. Especially, it shows a stronger absorption at the relatively high frequency region as expected in the 1-D simulation and the theory. Since a 2-D time domain simulation does not diverge over the frequency range from 240THz to 780THz, it is proven that the proposed QCRF dispersive FDTD does not suffer any numerical stability issues in the 2-D simulation over a certain frequency range. It should also be mentioned that if the QCRF dispersive FDTD simulation is

performed at an unintended frequency, the stability can not be guaranteed and the simulation may diverge.

3.4 3D

In this section, QCRF-based dispersive FDTD will be compared with non-dispersive FDTD on a 3D geometry. As shown in Fig. 3.10, the simulation is performed on the 3-D space (40x40x120 cells) and a cubic-shaped QCRF/a-Si material (40x40x40 cells) is implemented at the center of the simulation region. The x and y boundary has a periodic boundary condition and the z boundary has 10 cells of a perfectly matched layer at the end of the z axis. If the structure does not have an x and y dependent in it, we can assume that the simulation result will be the same as the simulation done in an infinite x-y plane and with a z thickness. It should be mentioned that the input pulse is a plane wave source without phase, which can propagate along the +z and -z direction without any distortion in the x,y PBC structure. Further, the 3-D simulation result should be identical with the 1-D simulation which has the same thickness and geometry setting along the z axis of the 3-D geometry setting. At the end of this chapter, the 3-D dispersive simulation results will be compared with the 1-D dispersive simulation.

In the 3-D simulation, the source plane is located 30 cells away from the center of the QCRF/a-Si region. The first observation plane called 'Obs 1' is located at the upper region from the source plane and the second observation plane called 'Obs 2' is located at the center of the QCRF/a-Si region. In the non-dispersive FDTD simulation, a DC-offset sinewave is excited and many simulations are performed over the frequencies of interests. For the dispersive FDTD, two entire simulations have been performed in order to calculate the propagation loss. The first simulation was done in the free space and the second simulation was done with QCRF materials.

As shown in Fig. 3.11, dispersive FDTD simulation results, which are represented as a line, have good agreement with non-dispersive FDTD simulation results, which

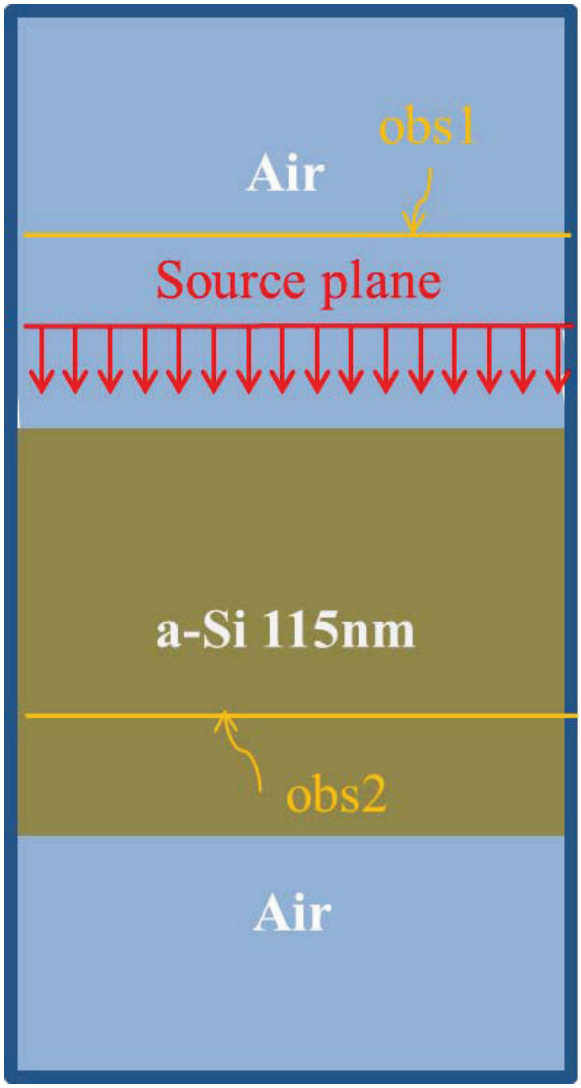

Fig. 3.10. Geometry setting for 3-D dispersive FDTD and non-disperisve FDTD simulation. The x and y edges are periodic boundary condition and the z edges have a perfectly matched layer. 'Obs1' means observation plane 1 which is located at the upper side of the source plane and 'Obs2' means observation point 2 which is located inside the QCRF material.

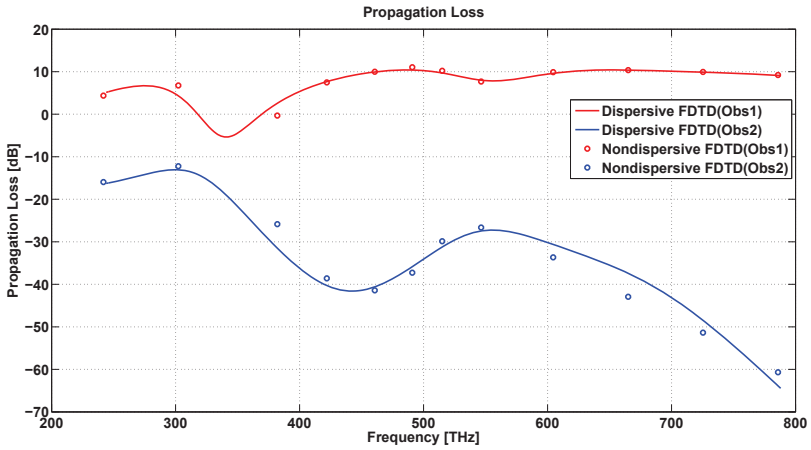

Fig. 3.11. 3D FDTD simulation result with dispersive FDTD and non-disperisve FDTD. The line represents dispersive FDTD and a dot represents a non dispersive FDTD. The color red represents observation plane 1 and color blue represents observation plane 2.

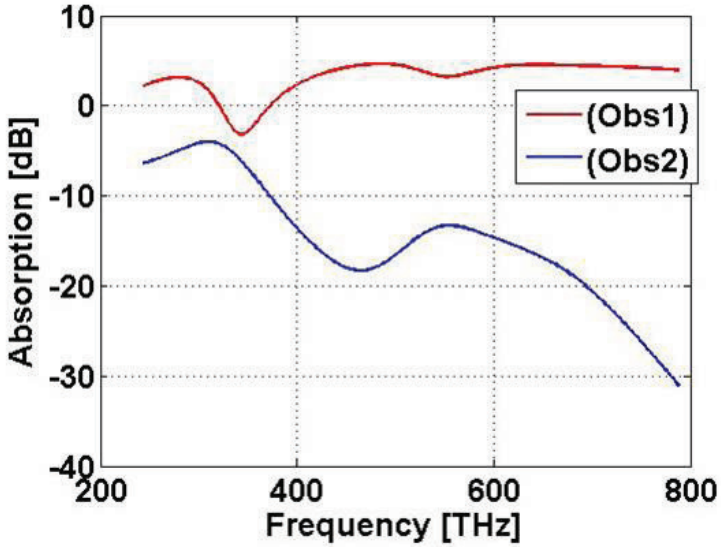

Fig. 3.12. 1D FDTD simulation result with dispersive FDTD. The red line represents observation plane 1 and the blue line represents observation plane 2. The geometry of this simulation is identical with the 3D geometry setting.

are represented as a dot. The y axis of Fig. 3.11 is the same as that of Fig. 3.9. Since the plane wave source propagates along the +z, -z direction simultaneously, the propagation loss can be positive at the air region as shown in observation plane 1 of Fig. 3.11. To be specific, the free space simulation initially generates a certain amount of field intensity observed at 'Obs1' and 'Obs2'. These field intensities in both observation plane 1 and 2 should be identical in free space simulation. For the simulation with the proposed QCRF material, the same amount of input pulse will first be observed at the 'Obs1' and then a reflected field will be observed next, which means the propagation loss can be positive only at 'Obs1'. As shown in Fig. 3.11, the non-dispersive FDTD simulation also shows a positive propagation loss at 'Obs1'. At 'Obs2', field intensity is substantially decayed, which means the QCRF material has strong light absorption.

As mentioned earlier, 3-D FDTD simulation, which has a x-y periodic boundary condition, should generates the same results as with the 1-D simulation. In order to

confirm this identity, 1-D simulation was performed with a simulation domain of 120 cells . As shown in Fig. 3.12, the 1-D simulation results are very similar to the 3-D simulation results. The trend and shape of the 3-D propagation loss curve agrees well with those of the 1-D absorption curve.

In conclusion, the proposed QCRF based dispersive FDTD shows very good agreement with dielectric slab theory and non-dispersive FDTD, which are already proven thru much past researches. The QCRF dispersion model, however, covers the frequency range that is denoted in this simulation, so if we want to extend the frequency range of a QCRF based FDTD simulation, the QCRF coefficients should be adjusted with measurement data that has a wider data set.

3.5 Comparison simulation results to analytic absorption

In the presence of single dielectric slab, the 3-D FDTD simulation results will be compared to analytic absorption derived by following equations [44]:

$$\rho_1(z) = \frac{\rho_1 + \rho_2 z^{-1}}{1 + \rho_1 \rho_2 z^{-1}} \tag{3.15}$$

where ρ_1 is the reflection coefficient at the left boundary, ρ_2 is the reflection coefficient at the right boundary as denoted in the Fig. 3.13. The eq. 3.15 represents analytic reflection using power series of z^{-1}. Since we can calculate easily the reflection coefficient from the right of the first interface by the fact that $\tau_1 = 1 + \rho_1$ and $\tau_1^{'} = 1 + \rho_1^{'}$, the above power series can be represented as a function of frequency [44]:

$$\rho_1(\omega) = \rho_1 + \sum_{n=1}^{\infty} \tau_1 \tau_1^{'} (\rho_1^{'})^{n-1} \rho_2^n e^{-j\omega nT} \tag{3.16}$$

Basically, an incident light reflected at the surface between air and dielectric slab at t= 0. At the surface, certain amount(ρ_1) of light reflected and rest(τ_1) of light transmitted at the boundary. By the eq. 3.16, we can predict the frequency domain

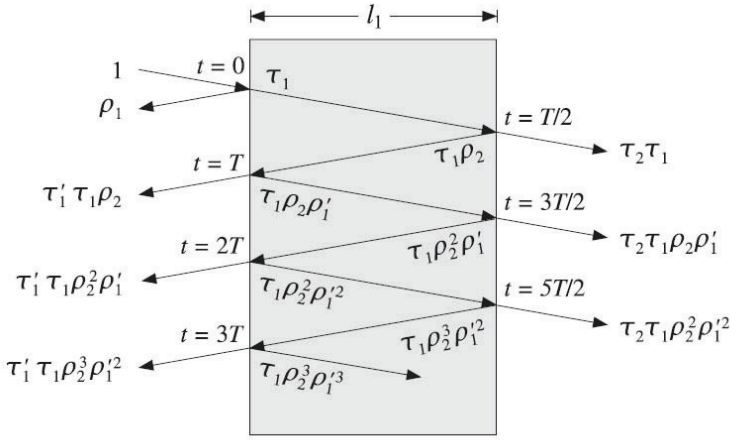

Fig. 3.13. Multiple reflections building up the reflection and transmission responses [44].

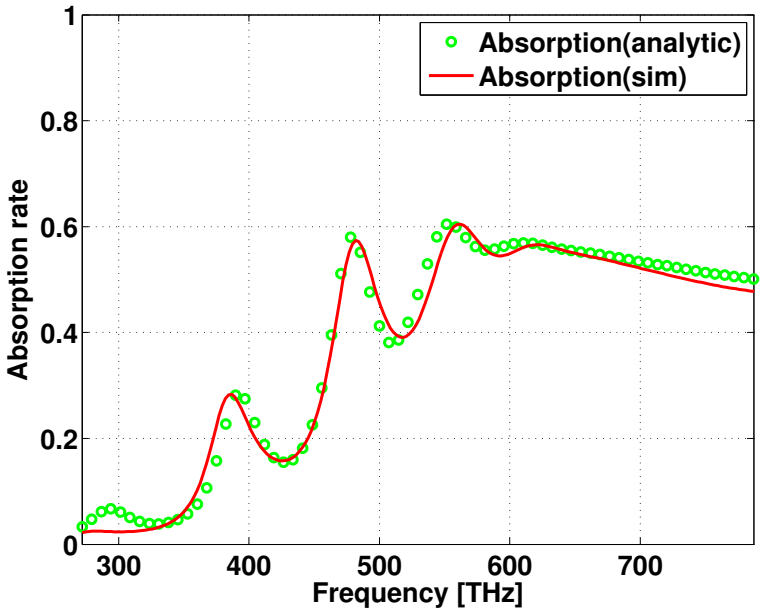

Fig. 3.14. Analytic absorption and simulation results in the presence of 300 nm dielectric slab of a-Si.

response by using power series. As a result of power series, the total transmitted wave can be obtained by the equation [44]:

$$\mathcal{T}(\omega) = \frac{\tau_1 \tau_2 e^{-j\omega T/2}}{1 - \rho_1' \rho_2 e^{-j\omega T}} = \frac{\tau_1 \tau_2 e^{-j\omega T/2}}{1 + \rho_1 \rho_2 e^{-j\omega T}} \tag{3.17}$$

In a similar way, we can derive the overall reflected response. As a result, the absorption of 300 nm dielectric slab of a-Si is derived. Also, the 3-D QCRF based FDTD simulation is performed with 300 nm thickness of a-Si material. As shown in Fig. 3.14, the simulation result predicts absorption of a-Si material very well. The simulation result also captured the Fabre-Perot oscillation occured in the dielectric slab.

3.6 Comparison simulation results to an experimental data

In this section, the 3-D FDTD simulation will be performed at the c-Si single junction solar cell structure, which is explained in the article [45]. Unlike amorphous silicon, crystalline silicon absorbs light between 400 and 1100 nm wavelength.

In the reference article, the authors mentioned that the thickness of c-Si layer was 1500 nm. In the presence of the anti-reflecting coating and the front glass, we performed a simulation with the same geometry setting which is explained in the experiment [45].

As shown in Fig. 3.15, the absorption rate of a red curve which is denoted as flat structure, is similar with our simulation result shown in Fig. 3.16. There is slightly different Fabry Perot oscillations are observed inside the thin film. This is because the size of front glass is much thinner in the simulation, compared to the experiment. The comparison result indicates that our simulation is not far from the real experiment as well as theory.

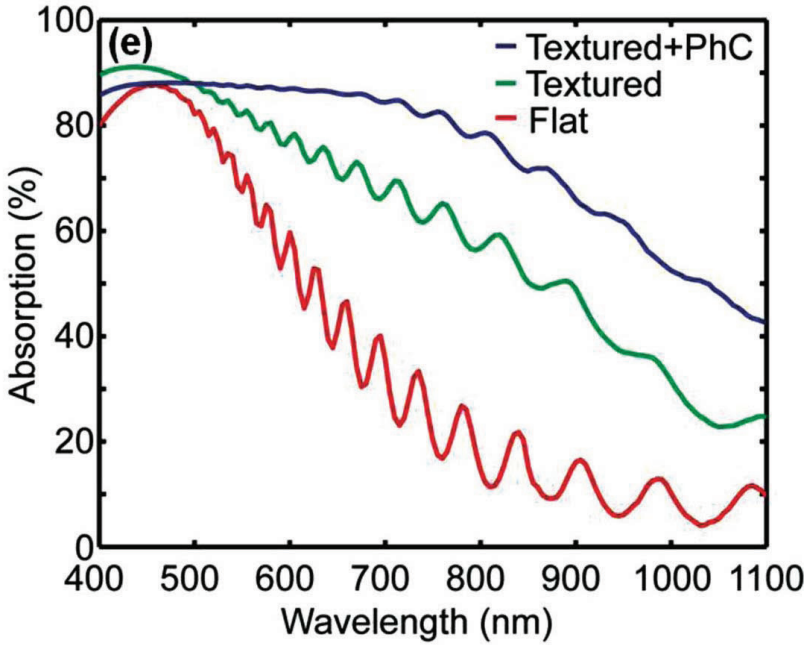

Fig. 3.15. Experimental absorption data with 1500 nm thickness of c-Si from the reference article [45].

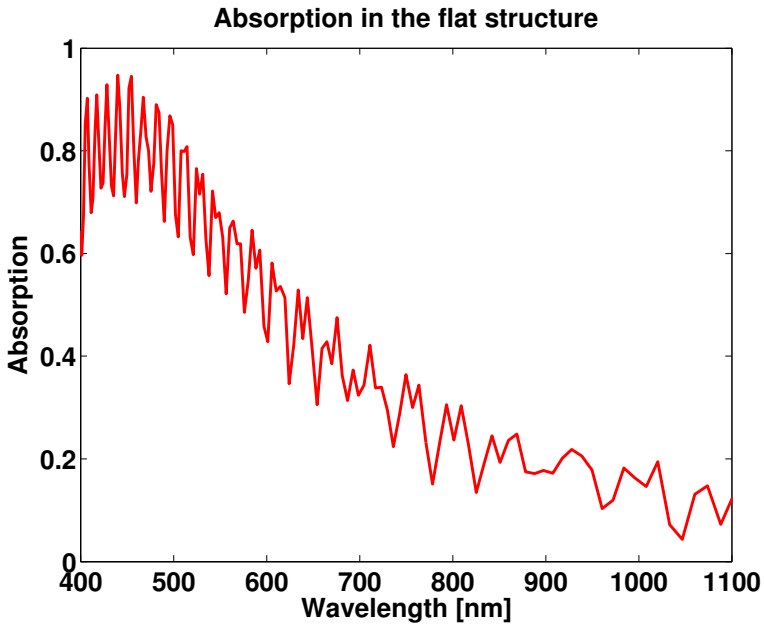

Fig. 3.16. Simulation absorption data with 1500 nm thickness of c-Si.

4. LIGHT TRAPPING METHOD IN AMORPHOUS SILICON BASED THIN FILM SOLAR CELL

Understanding the flow of light is very important in a photovoltaic (PV) cell. Because of incomplete light absorption, many PV cells have lower performance than the theoretical Shockley-Queisser limit [46]. This is particularly a challenge for thin-film materials with low mobilities. Identifying the best light-trapping structures possible is very important to help maximize the performance and reduce the costs of PV cells. Light trapping can be achieved by changing the angle of the light as it travels in the solar cell, i.e., by elongating the length of the optical path, and this can be done by having a surface that has a rough texture. Theoretically, a rough-textured surface reduces reflection by increasing the probability that the reflected light will bounce back onto the surface, minimizing it from reflecting out of the cell. From early theoretical work on PV cells [47], [48], it is known that a perfectly random structure can scatter light at all possible angles inside the active layer, which can enhance the absorption (effective path length) up to $4n^2$. However, thin-film solar cells, in particular, rarely achieve such high performance. Analytical approaches do not adequately describe real structures that can be built experimentally. In particular, the feature size of a randomly-textured surface seems to have an important role for light absorption. Although experiments are the ultimate guide, examining and optimizing a wide range of structures is extremely expensive and time-consuming. Thus an extremely accurate, simulation-based approach is needed to help guide experimentalists.

4.1 Efficiency of a Solar Cell

The efficiency with which a solar cell converts incoming photons into electricity is given in terms of the parameters of its electrical circuit [49]:

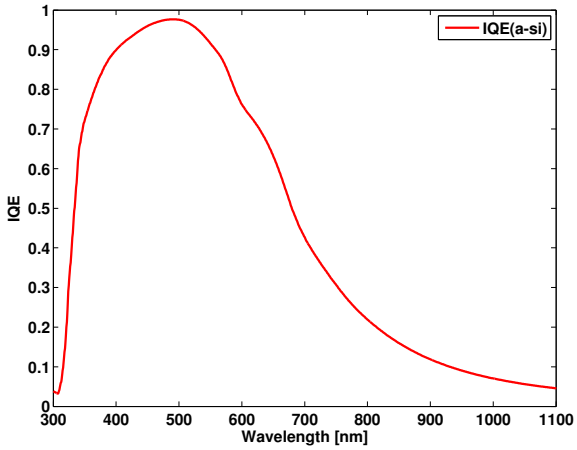

Fig. 4.1. Internal quantum efficiency curve of a-Si obtained from ADEPT simulator [53]

$$\eta = \frac{J_{sc} V_{oc} FF}{P_{in}} \tag{4.1}$$

where J_{sc} is the short-circuit current density, V_{oc} is the open circuit voltage, FF is the fill factor, and P_{in} is input power. The short-circuit current density depends directly on the degree of absorption of the incoming light, and it is given by [50]:

$$J_{sc} = \int_{\lambda 1}^{\lambda 2} d\lambda [\frac{e\lambda}{hc} \frac{dI}{d\lambda} A(\lambda) IQE(\lambda)] \tag{4.2}$$

where $A(\lambda)$ is the absorption rate of solar cell, $IQE(\lambda)$ is the internal quantum efficiency (as depicted in Fig. 5.1), $\frac{dI}{d\lambda}$ refers to the light intensity to which the solar cell is exposed per unit wavelength (given by the ASTM AM1.5 solar spectrum as shown in Fig. 4.2 [51]), where e is the elementary charge of an electron, h is the Planck constant, and c is the speed of light. In this study, we assumed that each absorbed photon with energy greater than the band gap energy generates an electron-hole pair with a probability of reaching the electrical contacts given by the internal quantum efficiency at that wavelength $IQE(\lambda)$ [52]

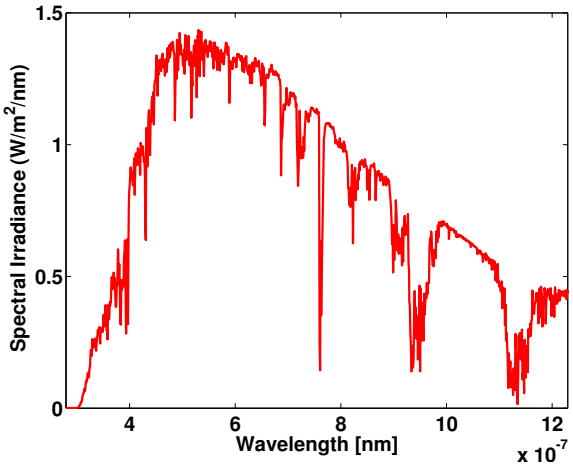

Fig. 4.2. ASTM AM1.5 solar spectrum

4.2 Definition of light absorption in time domain simulation

As explained in eqs. 4.1 and 4.2, overall efficiency of a PV cell depends on the absorption and the IQE of a certain structure. Since IQE does not change significantly with different surface roughnesses, in this section, the focus is on investigating the rate of absorption of incident light.

The most common task of FDTD simulation is computing the transmission and scattering spectra from some finite structure. The procedure of computing reflected and transmitted power will be explained with by a well known FDTD tool, called MEEP reference page [54]. One could try to compute the fields and transmitted flux for each frequency separately. However, since we have a broad-spectrum dispersion model called QCRF for the novel photovoltaic materials as suggested in the previous chapter, it is possible to obtain the broadband spectrum of the reflected flux and the transmitted flux with a single computation.

For example, one may want to calculate the power transmitted through a certain structure. For a given frequency, this can be done by integrating the Poynting vector over a plane that is defined as the flux plane.

$$P(\omega) = \Re[\overrightarrow{n} \dot{\int} [E^*_\omega \times H_\omega(x) d^2x] \tag{4.3}$$

Now, after an input pulse is exited into the structure, one may try to integrate the Poynting vector in the time domain, and then use a Fourier transform to convert the time domain Poynting vector $P(t)$ to the frequency domain Poynting vector $P(\omega)$. However, this approach does not produce the desired result because the calculation produces the Fourier transform of the flux instead of the flux of the Fourier-transformed field E and H. In order to obtain the flux of the Fourier-transformed field E and H, one should accumulate the Fourier transforms of the E and H field over the entire flux plane for each time step.

$$\tilde{f}(\omega) = \frac{1}{\sqrt{2\pi}} \sum_n e^{i\omega n\Delta t} f(n\Delta t)\Delta t \approx \frac{1}{\sqrt{2\pi}} \int e^{i\omega t} f(t) dt \tag{4.4}$$

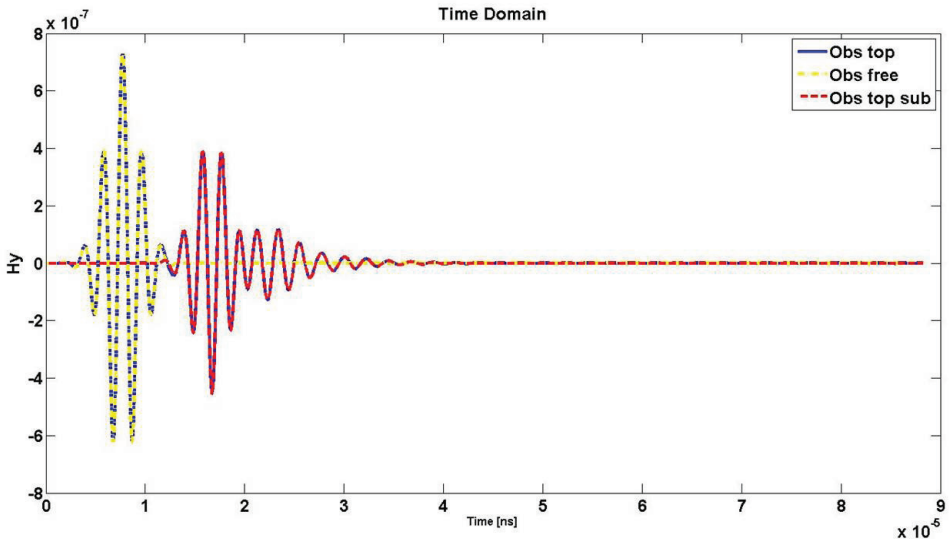

Fig. 4.3. Time domain signal observed at the top flux plane. The yellow curve indicates the pulse observed in the free-space simulation, the blue curve indicates the pulse observed at the simulation with the structure and the red curve represents the subtracted field.

After the time domain simulation has been completed, $P(\omega)$ must be computed by acquiring the cross product of the fluxes of the Fourier-transformed fields. The transmitted power and reflected power that are obtained are not very useful until they are normalized. As a normalization procedure, the reflected power and transmitted power are divided by the incident power at each frequency. Commonly, this procedure is done by running the simulation twice. The first simulation is done only with the incident pulse so that the incident power is calculated via the flux plane. The second simulation is done with the proposed structure with the same incident pulse.

Computing the reflected spectrum is more complicated. At the flux plane that calculates the reflected power, the incident pulse must be added in the reflected pulse. In order to avoid interference effects, the time-domain data of the incident field must be stored in memory at the first free space simulation, and then the stored time domain input pulse should be subtracted from the second simulation to get the

correct reflected power. The subtracted time-domain signal is illustrated in Fig. 4.3. The yellow curve is the time-domain pulse observed at the flux plane in the free space simulation and the blue curve is the time-domain pulse observed at the same flux plane in the simulation with the structure. Basically, the blue curve includes the yellow curve in it at the initial time steps and then the reflected time domain signal is observed after. After subtracting the yellow curve from the blue curve, the red curve is left, which represents reflected pulse observed at the upper flux plane. This procedure can be written as:

$$P_r(\omega) = \Re[\overrightarrow{n}\dot{\int}[E_\omega(x) - E_\omega^{(0)}]^* \times [H_\omega(x) - H_\omega^{(0)}(x)]d^2x] \tag{4.5}$$

where $E_\omega^{(0)}$,$H_\omega^{(0)}$ are the intensity of the incident fields observed at the flux plane. Finally, the absorption rate is defined as:

$$A = 1 - \frac{P_t(\omega)}{P_0(\omega)} - \frac{P_r(\omega)}{P_0(\omega)} \tag{4.6}$$

where A is the absorption rate, $P_t(\omega)$ is the transmitted power, $P_r(\omega)$ is the reflected power and $P_0(\omega)$ is the incident power. In Fig. 4.4, the blue curve indicates the incident power, the red curve indicates the reflected power and the green curve represents the transmitted power. The above equation can be written more simply as:

$$A = 1 - T - R \tag{4.7}$$

where T is the normalized transmitted power and R is the normalized reflected power. Once the absorption rate of a certain structure is obtained with FDTD simulation, J_{sc} and η can be calculated by following the procedure mentioned earlier.

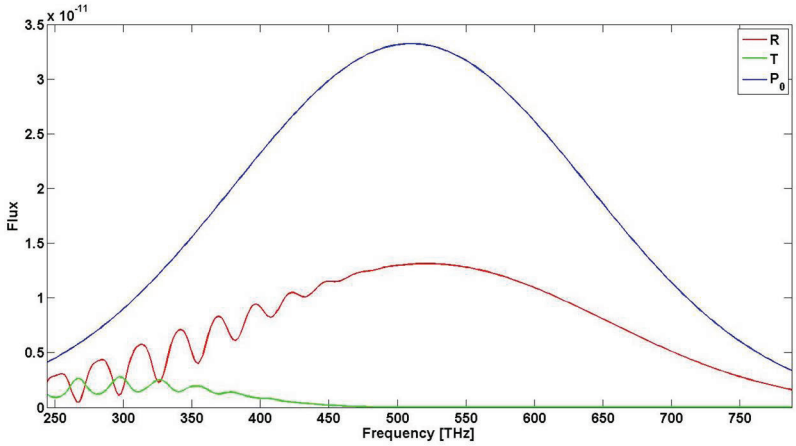

Fig. 4.4. Simulation of the reflected, transmitted and incident fluxes

4.3 Statistical random surface texturing

Thin-film amorphous silicon-based solar cells have operated far from the Shockley-Queisser limit in all experiments to date. However, the novel light-trapping structures suggested in this section, may help address this limitation. Recently, broad ways of texturing methods have been applied to the thin film solar cell [56]. Also, the characteristic of amorphous silicon has been researched aggressively [57, 58] .In this section, a statistical correlated random surface-texturing model is suggested as a novel light trapping method.

Basically, the proposed model has both periodicity and randomness. The idea of randomness with some correlation factor starts from the following equation:

$$Z_{n+1} = f * Z_n + \sqrt{1 - f^2} * r_n \tag{4.8}$$

where $Z_1 = r_1$, r_n is an independent sampling from a random distribution of Gaussian variables with zero mean and unit variance and f is correlation factor which has a value from 0 to 1. When f is equal to 0, a flat surface is generated. Since we are going to use this randomly generated surface in the 3-D FDTD simulation, which has a periodic boundary condition at the x-y edges, the periodicity at the left edge and right edge should be considered in this correlation function.

$$Z_{n+1} = f * Z_n + f^{N-n-1} * Z_N + \sqrt{1 - f^2 - f^{2(N-n-1)}} * r_n \tag{4.9}$$

where N is the maximum index of the 1-D structure. Now, eq. 4.8 is expanded to a double-sided correlation function as shown in eq. 4.9. The application of the double-sided correlation function ensures that the textured surface will not have abrupt changes of a height at its edges. As a result, a random surface with a double correlation is generated in 1-D space. As shown in Figs. 4.5 and 4.6, the curves in the figures have periodicity at the edges and randomness along the grids. These two 1-D random texturing curves are used as the boundaries of the 2-D random surface.

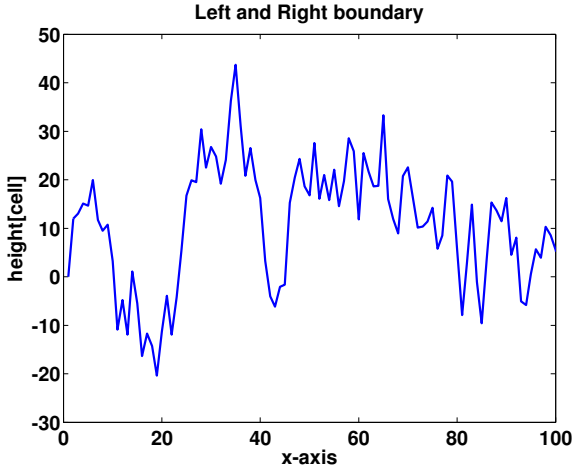

Fig. 4.5. Left and right boundaries of a 2-D random surface. x-axis denotes position of x-direction.

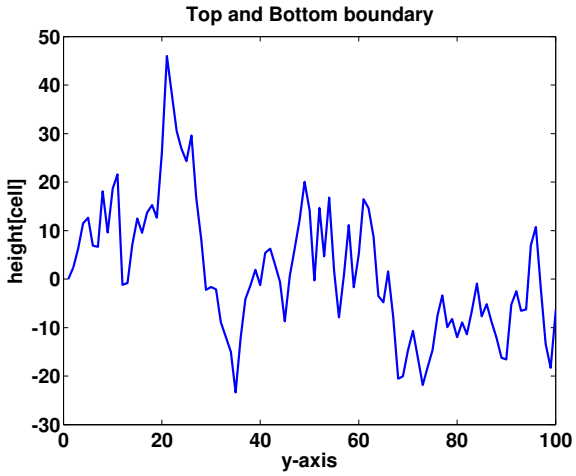

Fig. 4.6. Top and bottom boundaries of a 2-D random surface. y-axis denotes position of y-direction.

The double-sided correlation equation is now expanded in the 2-D surface. Initially, the heights of the four corners were fixed as zero in order to make sure the surface had periodicity at the x-y plane. Also, the left boundary has the same features as the right boundary as shown in Fig. 4.5, the upper boundary has same features as the lower boundary, as shown in Fig. 4.6. The internal architecture of the random surface is generated by following equation:

$$\begin{aligned} Z_{i+1,j+1} = & \, w(i, N_i) * Z_{i,j+1} \\ & + (f/2 - w(i, N_i)) * Z_{N+2-i,j+1} \\ & + w(j, N_j) * Z_{i+1,j} \\ & + (f/2 - w(j, N_j) * Z_{i+1,N+2-j} \\ & + \sqrt{1 - f^2} * r_n \end{aligned} \tag{4.10}$$

where i represents the x index, j represents the y index, N_i is the maximum index of i and N_j is the maximum index of j and $w()$ denotes a weighting function:

$$w(i, N) = f/2 - (f/4) * \exp(-(N - 2 * i + 2)). \tag{4.11}$$

Using eq. 4.10, we can create the internal architecture with an alternating order. Simply speaking, the randomly-textured surface is generated by the following algorithm:

1. Fixing $Z(0,0)$, $Z(0,N)$, $Z(N,0)$, $Z(N,N)$.
2. Generating its boundary with eq. 4.9.
3. *while*$(n < N/2)$ 3a. Generating from $Z(n,n)$ to $Z(n, N-2n+1)$ with eq. 4.10
3b. Generating from $Z(N-2n+1, n)$ to $Z(N-2n, N-2n+1)$ with eq. 4.10
3c. Generating from $Z(n,n)$ to $Z(N-2n+1, n)$ with eq. 4.10
3d. Generating from $Z(n, N-2n+1)$ to $Z(N-2n+1, N-2n+1)$ with eq. 4.10

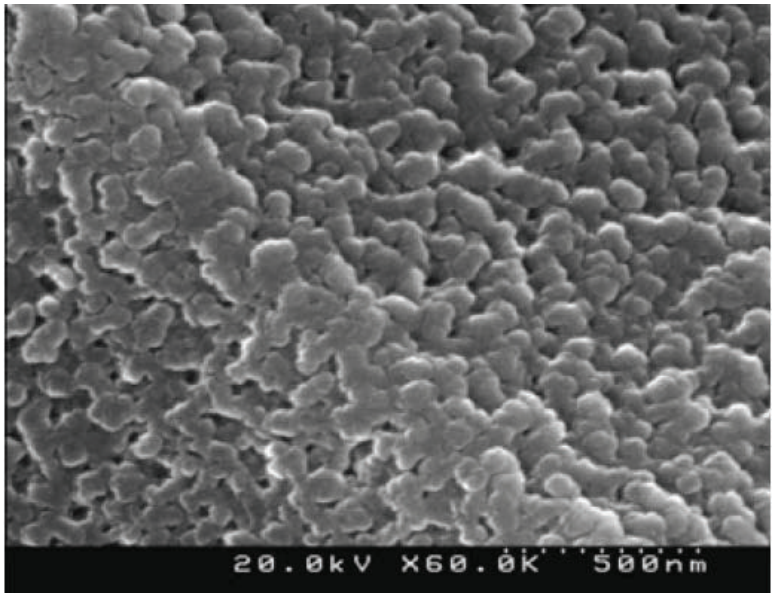

Fig. 4.7. Plan view SEM image of porous silica AR layer formed by vapour-etch method [56].

As a result of this algorithm, a randomly-textured surface having the desired correlation factor was generated, as shown in Figs from 4.8 to 4.11. Our texturing method is compared with the recent studies from reference paper [56]. As shown in the Fig. 4.7, their texturing method shows many local peaks having 50 to 100 nm width. Among the variety of our random surface texturing samples, the sample with f = 0.99 matches well with the texture method introduced in the reference paper [56], in terms of the width of local peaks. Basically, it was found that the randomness was dominant when the correlation factor(f) was less than 0.75, as shown in Fig. 4.9. Looking at these surfaces, one hardly distinguishes which one will be the best light trapping structure among a variety of randomly-textured surface. It will become more apparent when these randomly-textured surfaces are applied to the 3-D FDTD simulation with the proposed dispersion model (QCRF).

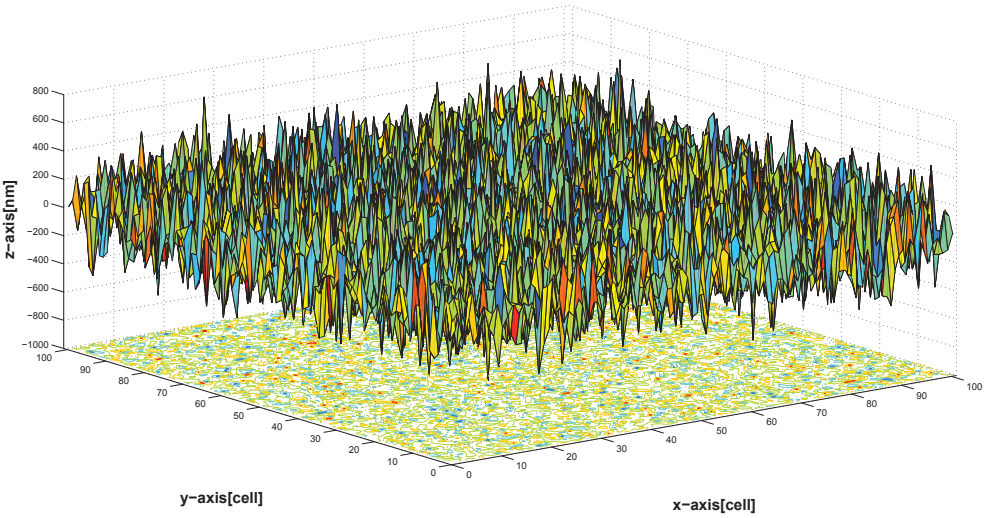

Fig. 4.8. Random surface texturing with the correlation number f = 0

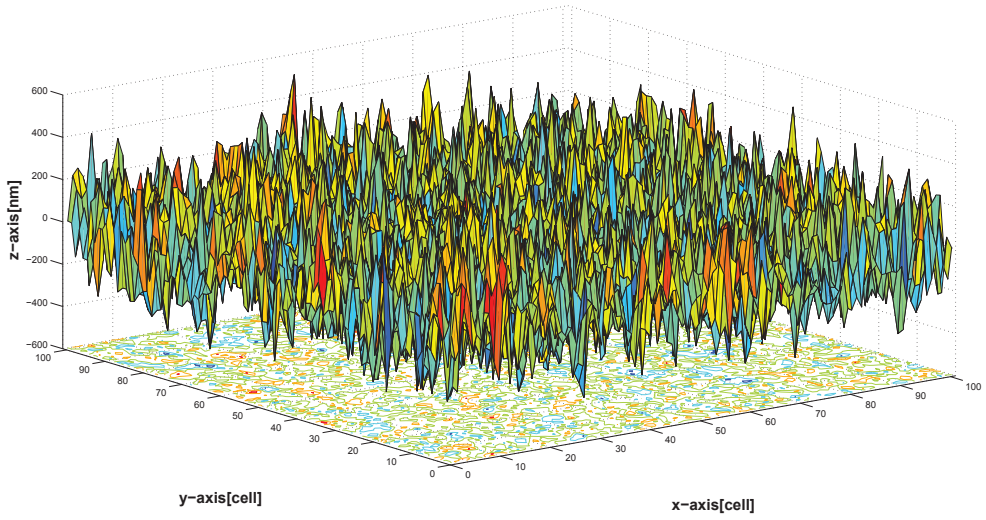

Fig. 4.9. Random surface texturing with the correlation number f = 0.75

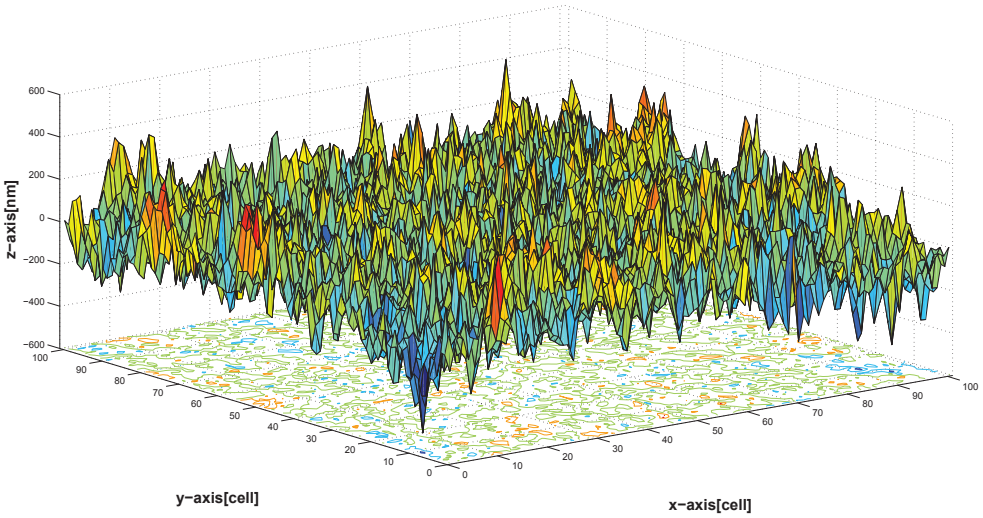

Fig. 4.10. Random surface texturing with the correlation number f = 0.90

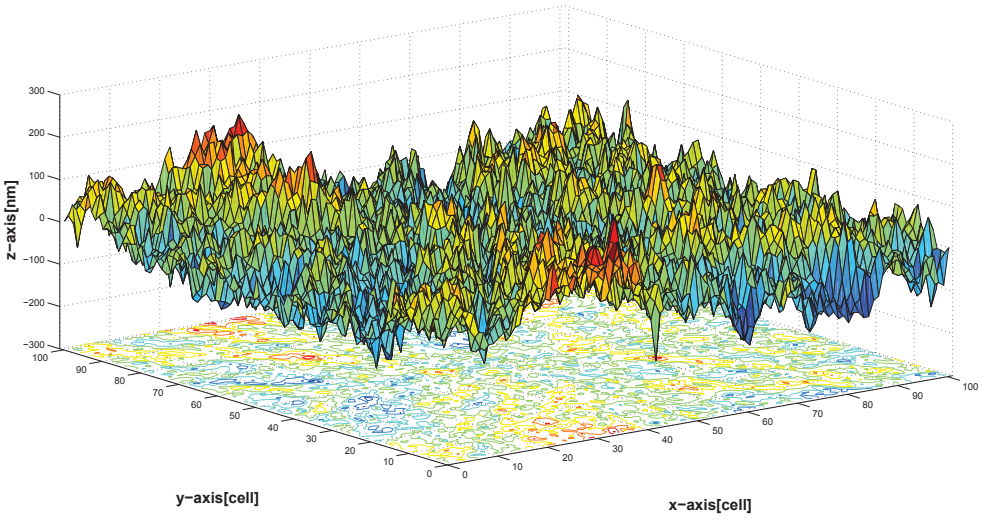

Fig. 4.11. Random surface texturing with the correlation number f = 0.99

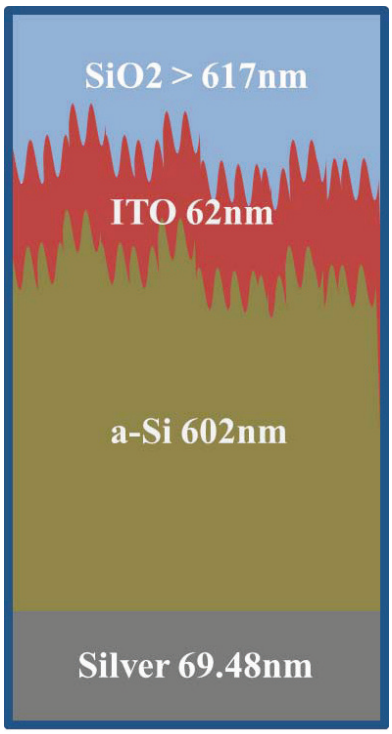

Fig. 4.12. A structure of single junction solar cell with a-Si

4.4 3-D FDTD simulation with variety of randomly textured structure

It is believed that the optimum light-trapping structure has a combination of randomness and periodicity. In this section, the optimum light trapping structure will be investigated via the randomly-textured surface obtained from the previous section. The 3-D QCRF-based dispersive FDTD will be performed with randomly-textured surfaces.

As shown in Fig. 4.12, the simulation was performed on the 3-D space (100 x 100 x 700 cells), and a QCRF/a-Si material (100x100x155 cells) was used inside. At the top of simulation region, glass(SiO2) that was 617nm thick, was used, and the bottom of the glass was a textured surface. For an anti-reflection coating, a 62nm-thickness of ITO layer was used under the glass region with the same shape as the textured surface. Following the ITO-textured surface, a QCRF/a-Si layer was used, which

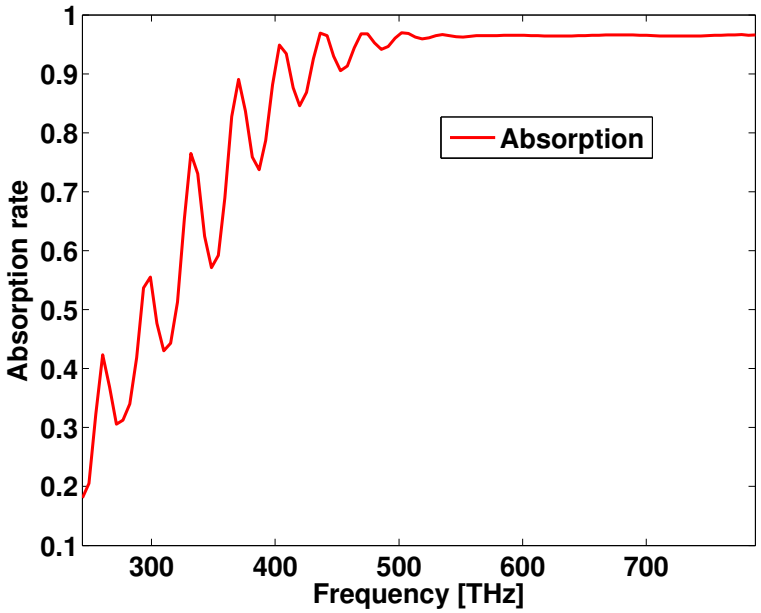

Fig. 4.13. Absorption of the proposed, randomly-textured structure with a correlation number of 0

had an average thickness of 600nm. A 69-nm-thick silver layer was used for back reflection. The a-Si layer and the silver layer were modeled by the QCRF dispersion model, and the other materials were modelled by a constant dispersion model, as explained in reference [8]. The grid spacing was fixed at 3.86nm per cell, because that ensures 20 Pixel Per one Wave(PPW) in the simulation. When the PPW of the simulation was significantly less than 20, numerical error became dominant, because the simulation was not able to discretize the waveform properly. Also, the x and the y boundaries had a periodic boundary conditions, and the z boundary had 10 cells of a perfectly-matched layer at the end of the z axis. The incident pulse was excited at the upper region of the glass layer, which was a vacuum in this simulation.

It can be assumed that this simulation was identical to an infinite x-y plane with a periodicity of 386nm (3.86nm x 100 cells)along the x and y axes. The simulations were performed and the absorption rate was obtained via the procedure mentioned in the Efficiency of a Solar Cell section.

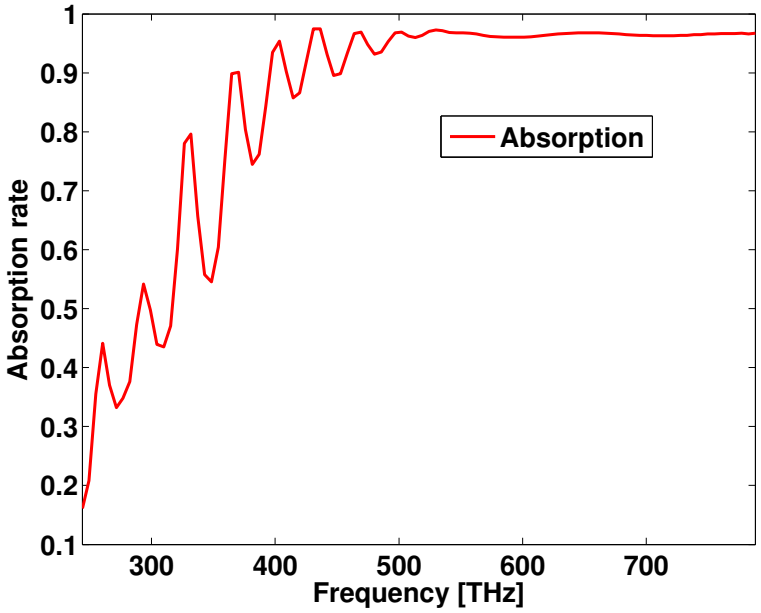

Fig. 4.14. Absorption of the proposed randomly-textured structure with a correlation number 0.75

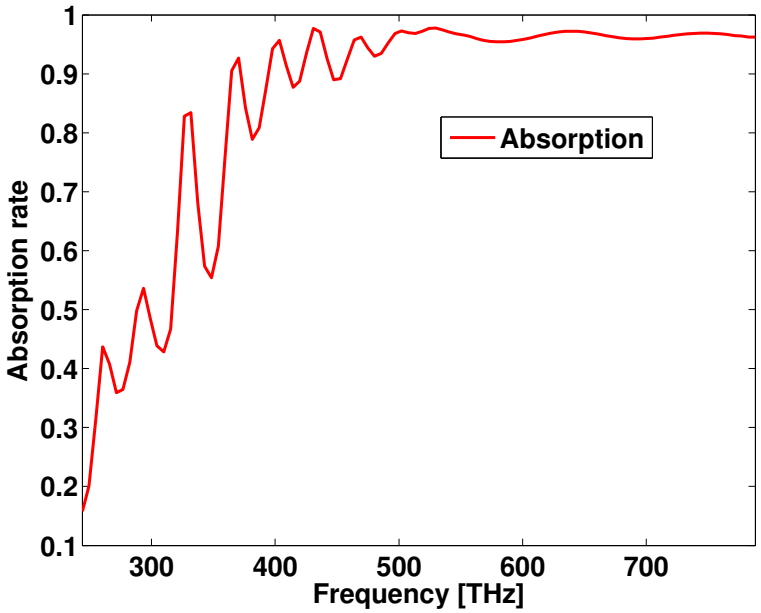

Fig. 4.15. Absorption of the proposed randomly-textured structure with a correlation number 0.90

As shown in Fig. 4.13, a totally random structure with a zero correlation factor had a relatively good absorption rate at the high frequency range. Among the four samples, the flat surface structure had the worst light absorption rate. It is not clear that Fig. 4.16 had better absorption rate compared to Fig. 4.15. However, if the absorption curves are quantized by multiplying the IQE data and the AM1.5 data, it will be confirmed that the correlation factor 0.99 is the optimum structure for a 600-nm thickness, a-Si single junction solar cell. Details of quantizing the absorption rate will be followed at the next chapter.

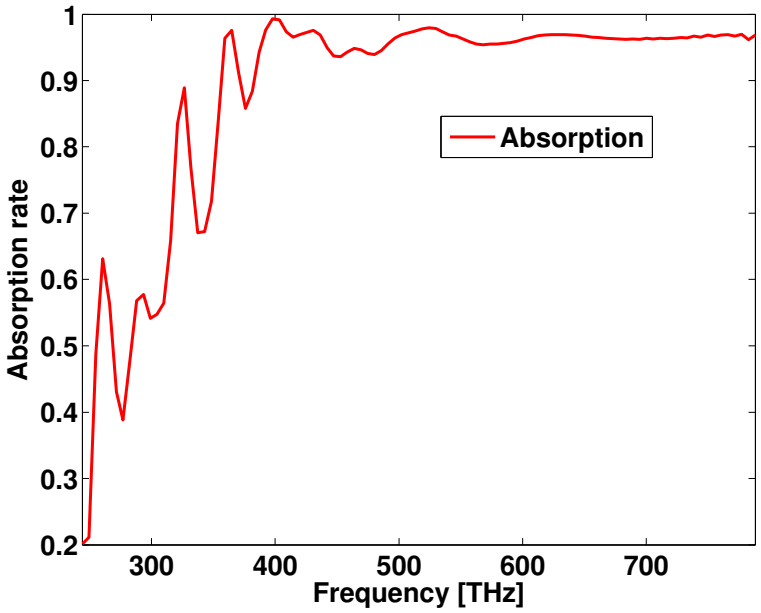

Fig. 4.16. Absorption of the proposed randomly-textured structure with a correlation number 0.99

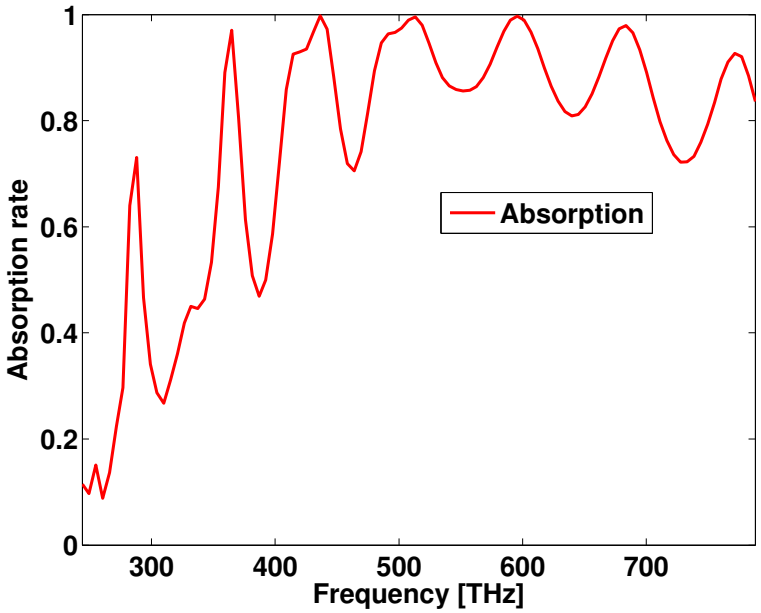

Fig. 4.17. Absorption of the proposed structure with a correlation number of 1 (flat surface)

5. DESIGN OPTIMIZATION: TANDEM CELL

Recently, an initial efficiency of 12.3% was achieved for a double-junction solar cell (a-Si/microcrystalline-Si) [59]. Also, many works have been done on silicon photovoltaic area, which are closely related to this study [60]. In this thesis, a front-texturing method was studied with a statistically-correlated model combined with full-wave, optical simulation. In order to obtain the optimum design, several design parameters were fixed as constants, i.e., internal quantum efficiency(IQE), dark current (J dark) and ideality factor (IF). As mentioned in chapter 4, the efficiency of a solar cell is defined as an integration of IQE, absorption and AM1.5 data [61]. AM1.5 stands for air mass 1.5 which is general reference of solar irradiation defined by the american society for testing and materials (ASTM). It is an open-source and anyone can download it. Also, IQE data for the a-Si layer and the c-Si layer were obtained in using ADEPT simulation [53]. ADEPT is drift-diffusion simulator developed in Purdue university. For the dark current, we used an approximation method that is represented by the following equation:

$$J_{dark} = J_{sc} \exp(\frac{-qV_{oc}}{nkT}) \tag{5.1}$$

where, J_{sc} is a short-circuit current [59], V_{oc} is the open-circuit voltage [59], n is the ideality factor [62], k is the Boltzmann constant and T is temperature in kenvin. The resulting dark currents for a-Si and c-Si were $8.0716 * 10^{-10}[mA/cm^2]$, and $3.3748 * 10^{-7}[mA/cm^2]$, respectively. Once the short circuit current was obtained from the FDTD simulation, the open-circuit voltage was calculated by the following equation [64]:

$$V_{oc} = \frac{nkT}{q} \ln(\frac{J_{sc}}{J_{dark}}) \tag{5.2}$$

where J_{dark} is the dark current obtained from eq. 5.1. Now, we introduce Z_{oc} which is adepted from the reference for single junction Zoc [64]:

$$Z_{oc} = \frac{V_{oc1}}{n_1 kT/q} + \frac{V_{oc2}}{n_2 kT/q} \tag{5.3}$$

where, V_{oc1} is the open-circuit voltage of a-Si layer, V_{oc2} is the open-circuit voltage of c-Si layer, n_1 is the ideality factor of a-Si and n_2 is the ideality factor of c-Si. Now, the fill-factor calculation can be performed with the Z_{oc} value [64]:

$$FF_0 = \frac{Z_{oc} - ln(Z_{oc}+0.72)}{Z_{oc}+1} \tag{5.4}$$

where FF_0 is the initial fill factor, Z_{oc} is the open-circuit impedance calculated from eq. 5.3. Now, we introduce a series resistance in order to obtain the proper fill factor [64].

$$FF_s = FF_0(1 - 1.1r_s) + r_s^2/5.4 \tag{5.5}$$

which is valid for $r_s < 0.4$, $V_{oc} < 10$. After optimizing for several values of series resistance, $r_s = 0.2075$ was selected, which shows the closest correlation with the experimental data. The final equation used to calculate the efficiency of the cell was exactly the same as eq.4.1.

Fig. 5.1 was obtained from the ADEPT simulation. The IQE data start at 300nm and go to 1100nm, which corresponds the wavelength range of the FDTD simulation. In order to obtain reasonable data, a filter layer of glass, which absorbs light at very low wavelength ranges, was implemented at the front, and it eventually resulted in a decrease of the IQE ratio at the intended frequency range. It should be mentioned here that the IQE curve showed very little variation when the difference in the thickness of the material was a few nanometers, i.e., about 30nm. This means that it is possible to assume that the IQE of each layer is constant in the optimization process that is performed in the next section.

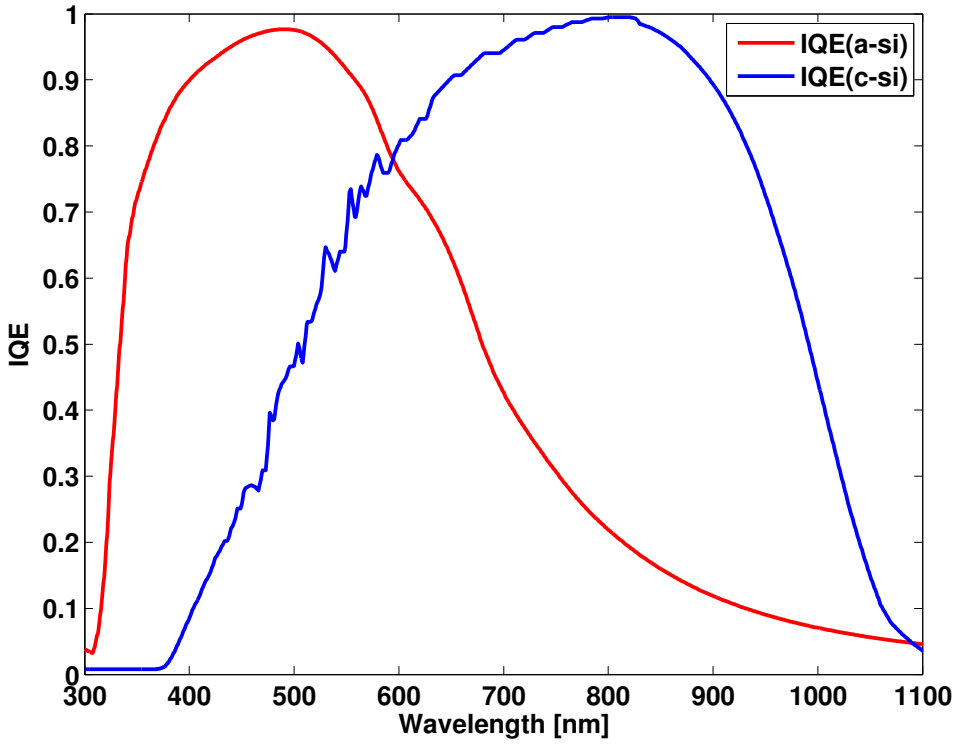

Fig. 5.1. Internal quantum efficiency of each layer obtained from ADEPT simulator [53]

5.1 Optimization in a flat surface structure

In this section, optimum thicknesses of the cells for each layer are investigated without using the light-trapping method. In this simulation, the efficiency of a cell was calculated by the following equation:

$$\eta = \frac{J_{sc}minV_{oc}FF}{P_{in}} \tag{5.6}$$

where $J_{sc}min$ is the minimum short-circuit current density between the two layers. In order to achieve the highest efficiency without using light-trapping techniques, current matching is very important. In this work, the thicknesses of the active materials were fixed to be a total of 2000 nm, which is summation of thicknesses of an a-Si layer and a c-Si layer. A range of different thickness for a-Si were considered. An a-Si acts like direct band-gap material with Eg= 1.73eV and a c-Si is indirect band-gap material where Eg= 1.12eV. Because of type of band-gap and filtering by a-Si in front, much greater c-Si thicknesses are needed for a proper light trapping design. The simulations were performed using flat surfaces, and there was no back-grating at the silver layer.

Fig. 5.2 shows the 3-D FDTD simulation that was performed, the rate of light absorption was calculated in the flux planes defined at the top, bottom, and internal-layers of the c-Si and a-Si. As expected, the front a-Si layer absorbed most of light at low frequency and the c-Si layer started receiving a non-vanishing amount of light starting from 450nm and dominated overall absorption for the wavelength higher than 600 nm. The short-circuit currents were obtained by multiplying the IQE curve and the absorption curves for each materials. Following the procedure mentioned earlier in this chapter, the open-circuit voltage, fill factor, and the efficiency of the cell were calculated. In other words, the optical simulation (FDTD) generates the normalized absorption rate and the semiconductor simulation (ADEPT) predicts IQE of each material.

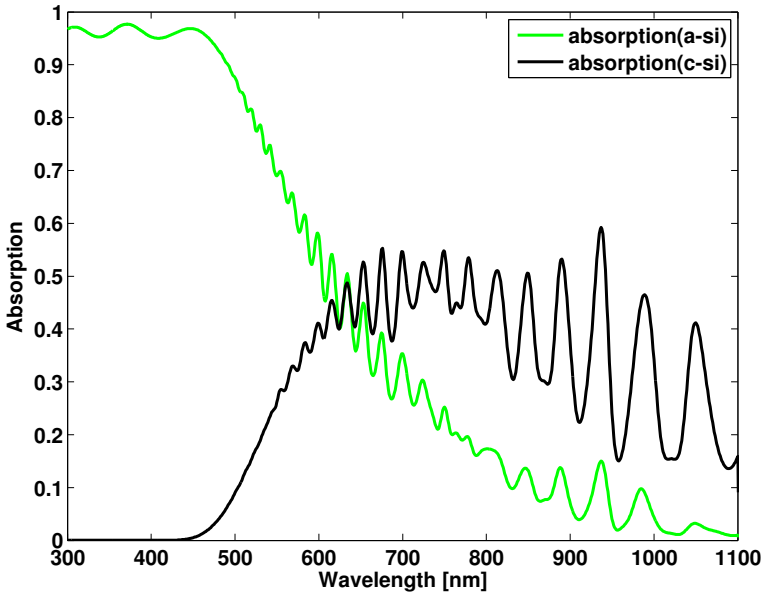

Fig. 5.2. Rate of light absorption for each layer in the 3-D FDTD simulation

Before optimizing the flat structure, we compared our procedure with the reference cell which is the highest efficiency tandem cell in the world [62, 63]. Since the reference paper didn't mention about the detail of their texturing method, we assumed a constant absorption rate which is 80% in this work. The Table 5.1 shows that our procedure is close to the realistic tandem cell operation in terms of the short circuit current density, the open circuit voltage and the fill factor.

As shown in Fig. 5.3 - 5.8, the optimum thickness of the a-Si layer was investigated. Basically, the short circuit current density of the a-Si layer increased as its thickness increased until it reached 220 nm. For thicknesses greater than 220 nm , the short-circuit current density decreased even though the thckness of the a-Si increased. Also, the short-circuit current density of the c-Si layer had its lowest peak at 220 nm. The overall efficiency had two peaks in the frequency range that was simulated in this chapter. The 250 nm/a-Si and the 1750 nm/c-Si structure had cell efficiencies of 9.83% were the best results among the simulations. The detailed simulation results are listed in Table 5.2.

Table 5.1
Comparison of our simulation model with the reference cell [62, 63]

Classification	Jsc(a-Si)[mA/cm^2]	Jsc(c-Si)[mA/cm^2]	Voc [V]	FF	η
Reference cell [62, 63]	12.93	12.93	1.365	0.6940	12.3 $\pm$ 0.3 %
Our simulation	12.9306	12.9300	1.3964	0.6927	12.5078%

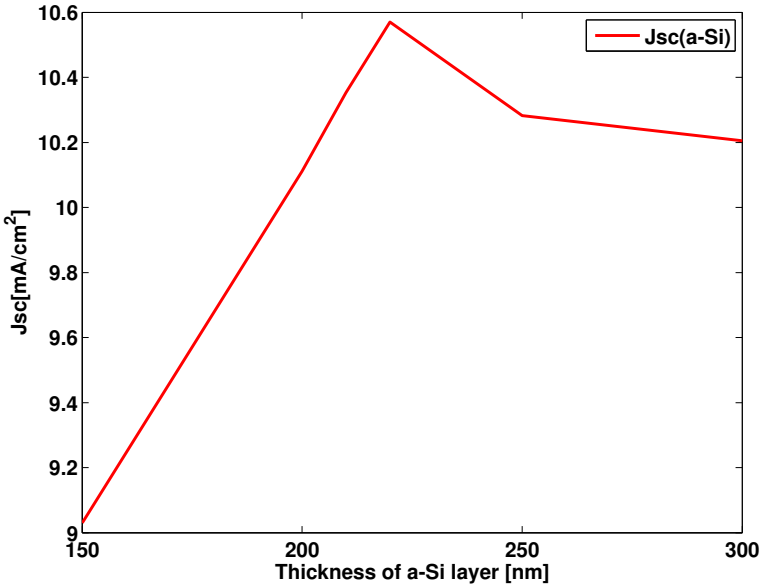

Fig. 5.3. Short circuit current density of a-Si layer with varying thickness of a-Si layer

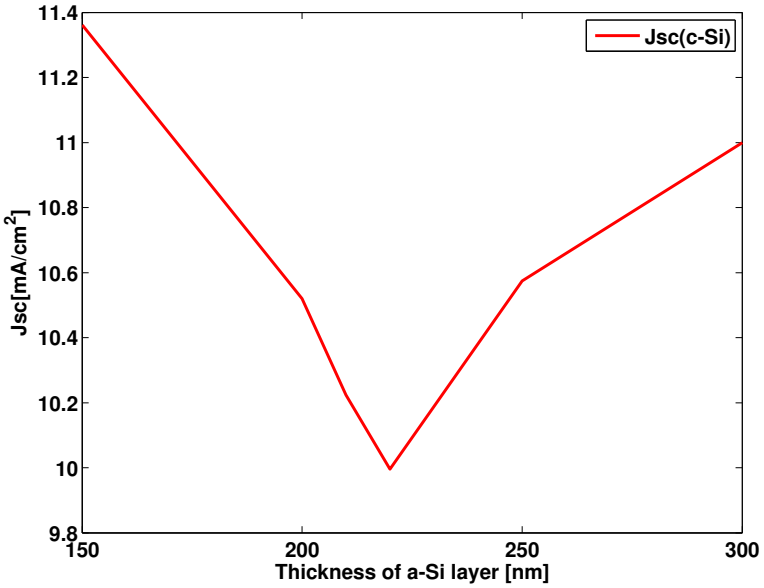

Fig. 5.4. Short circuit current density of c-Si layer with varying thickness of a-Si layer. Fabry-Perot oscillations account for higher Jsc even when a-Si thickness increases

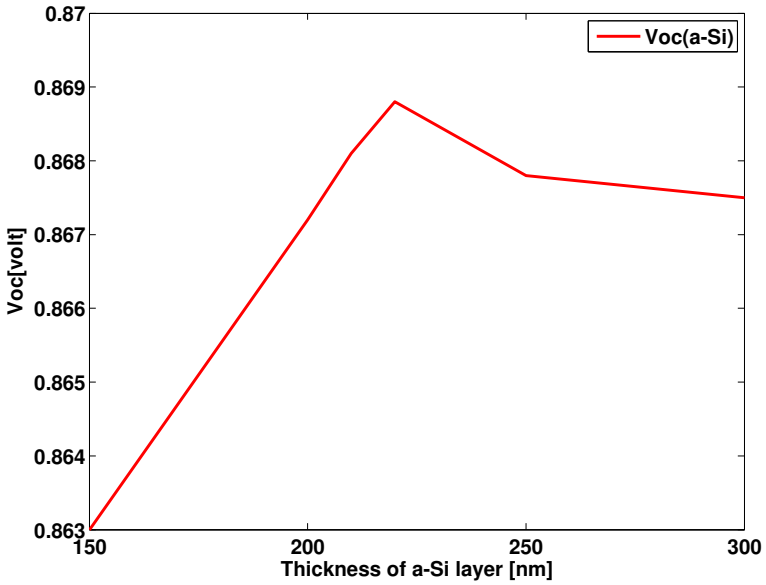

Fig. 5.5. Open circuit voltage of a-Si layer with varying thickness of a-Si layer

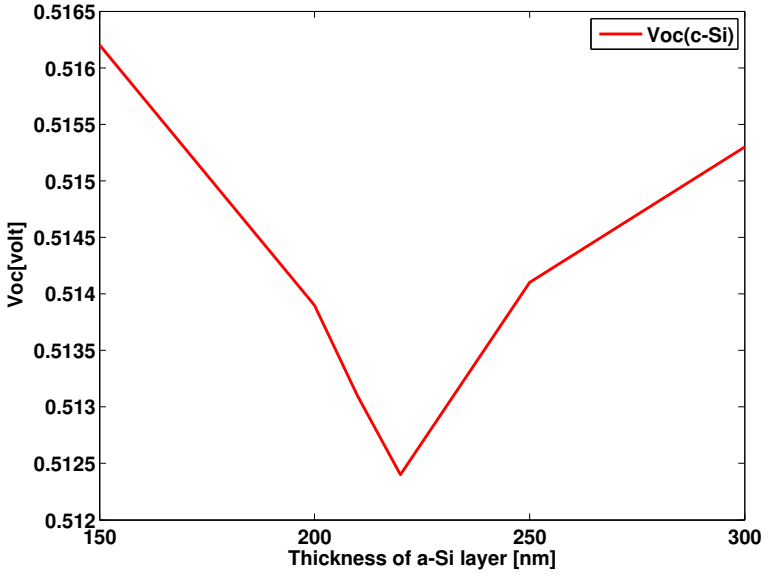

Fig. 5.6. Open circuit voltage of c-Si layer with varying thickness of a-Si layer. Fabry-Perot oscillations account for higher Voc even when a-Si thickness increases

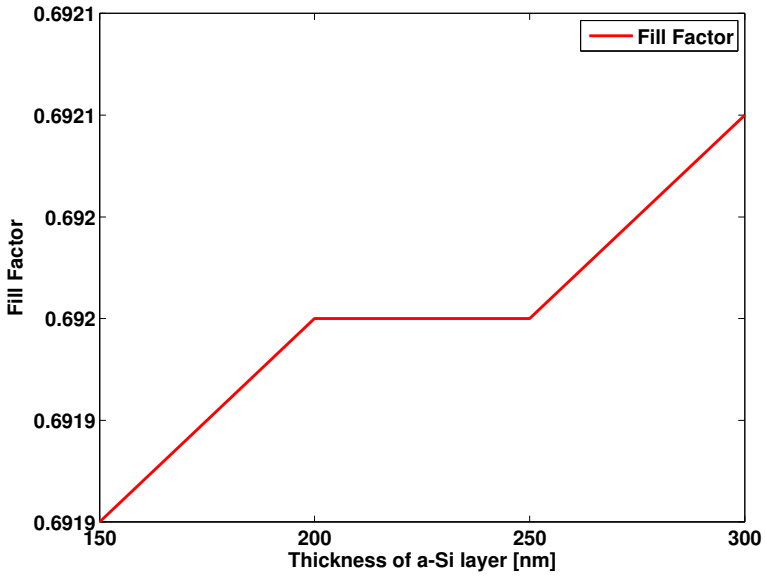

Fig. 5.7. Fill factor with varying thickness of a-Si layer

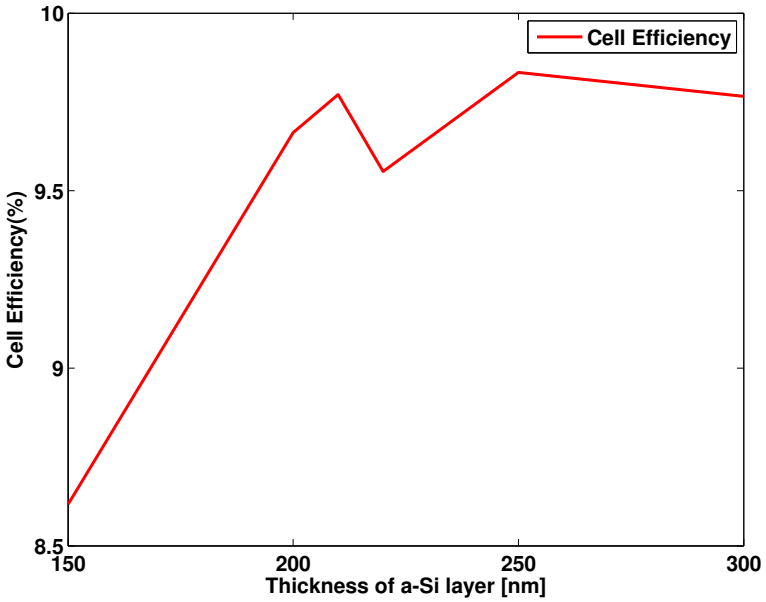

Fig. 5.8. Cell efficiency with varying thickness of a-Si layer

Table 5.2
3-D FDTD Simulation results. For a flat structure, it was found that 250 nm of a-Si and 1750 nm of c-Si gave the highest overall power conversion efficiency of 9.83 %

d1(a-Si)[nm]	d2(c-Si)[nm]	Jsc(a-Si)[mA/cm^2]	Jsc(c-Si)[mA/cm^2]	Voc(a-Si) [V]	Voc(c-Si) [V]	FF	η
150	1850	9.0303	11.3618	0.8630	0.5162	0.6919	8.6175 %
200	1800	10.1109	10.5195	0.8672	0.5139	0.6920	9.6630%
210	1790	10.3528	10.2236	0.8681	0.5131	0.6920	9.7708%
220	1780	10.5701	9.9957	0.8688	0.5124	0.6920	9.5537%
250	1750	10.2826	10.5748	0.8678	0.5141	0.6920	9.8332%
300	1700	10.2046	10.9994	0.8675	0.5153	0.6921	9.7656%

5.2 Optimization with light trapping method

In this section, the textured surface that, was studied in the Chapter 4, is applied at the front of the tandem cell. A double-correlated, textured surface is used at the ITO and at the front of the amorphous silicon layer. Any other layers, as denoted in the Fig. 3.10, are assumed to be flat.

We investigated an optimum, tandem-cell design with several parameters, e.g., thicknesses of the layers, height of the random structure, and a correlation number(f). Computational time for this problem consisting of a million picels over 40000 time steps on a single processor was approximately 36 hours. As such, optimization was effected manually in the interests of rapid convergence to the optimal values.

As a result, the rate of light absorption was obtained for the optimum structure, which had an a-Si layer that was 200 nm thickness, a c-Si layer that was 1800 nm thickness, a correlation number $f = 0.99$, and a height of randomness of 300 nm. As shown in Fig. 5.9, the 3-D FDTD simulation indicated that the rate of light absorption and the overall curves were enhanced over that of the flat surface simulation shown in Fig. 5.2.

An pre-optimized, tandem-cell structure had 11.6% efficiency, as denoted in Table. 5.3. At the future, global optimization algorithm will be applied to optimize further with variety of design variables including thickness of each layer, maximum height of surface texturing and surface roughness. It also showed well-matched current density between the amorphous and crystalline silicon layers.

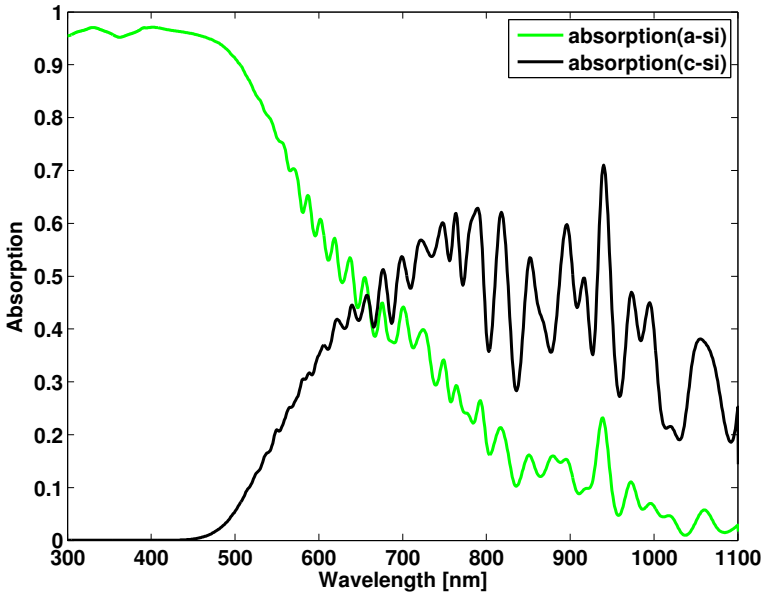

Fig. 5.9. Light absorption of an optimized tandem cell.

Table 5.3
3-D FDTD Simulation results. For a textured structure, it was found that 200 nm of a-Si, 1800 nm of c-Si and a single correlated surface gave the highest overall power conversion efficiency of 11.65 %

Texturing type	Correlation number	Jsc(a-Si)$[mA/cm^2]$	Jsc(c-Si)$[mA/cm^2]$	FF	η
Single correlation	0.800	11.0486	11.0268	0.6922	10.5783 %
Single correlation	0.900	11.2833	11.1150	0.6922	10.6714 %
Single correlation	0.950	11.4070	11.0839	0.6923	10.6437 %
Single correlation	0.990	11.4635	11.2904	0.6923	10.8483 %
Single correlation	0.995	12.5700	12.0701	0.6926	11.6473 %
Single correlation	0.999	11.4069	11.0839	0.6923	10.6437 %
Double correlation	0.800	11.1173	11.0255	0.6922	10.5784 %
Double correlation	0.900	11.2506	11.1425	0.6923	10.6971 %
Double correlation	0.950	11.2244	10.9962	0.6922	10.5526 %
Double correlation	0.990	11.3978	11.6308	0.6923	10.9577 %
Double correlation	0.995	11.1443	11.5444	0.6923	10.7049 %
Double correlation	0.999	10.3303	10.6784	0.6920	9.8824 %

6. CONCLUSION

Since silicon is the most abundant material in the world, it is commonly used in an inexpensive photovoltaic application. Compared to other PV materials, like GaAs, single junction a-Si solar cells have operated far from the Shockley-Queisser limit. In this thesis, we have suggested a novel light trapping structure utilizing a-Si material through time domain simulation of photovoltaic materials.

In order to properly capture the dispersion of real materials like silicon in the time domain, the QCRF dispersion model was suggested and parameters were optimized using the particle swarm optimization method. Its accuracy was verified by comparison to analytical data and it was applied to well known photovoltaic materials. Also, the QCRF method was enhanced by particle swarm optimization, which resulted in better accuracy and stability. The RMS error of PSO/QCRF curve fitting was 6.6(%), satisfying the Kramers-Kronig relationship. Using the proposed dispersion model, a full-wave optical simulation was performed in 1-D through 3-D. The simulation results showed that the proposed model (PSO/QCRF) predicts the absorption of light very well in the solar cell structure. It was also guaranteed stability in the 3-D dispersive FDTD simulation both theoretically and in simulations up to 40,000 time steps.

In this thesis, a statistically-correlated random surface-texturing model was suggested as a novel light-trapping method. The random-texturing model was applied to the front surface of a tandem cell structure and optimized with several design parameters. The proposed dispersion model was utilized to simulate the light trapping structure of the tandem cell, and it showed 11.6% cell efficiency, which was greater than that of the flat-surface simulation, which had an efficiency of 9.83%. This represents relative improvement of 18%.

In the future, a much broader range of light-trapping structures can be tested by the simulation method, researched and developed in this thesis. Also, the particle swarm optimization method will be applied to a design of tandem cell which has multiple continuous parameters to consider. Also, since this work as well as previous work verified that the QCRF model shows very good accuracy on modeling of a broad range of materials, it should be suitable to consider other well known photovoltaic materials e.g., CIGS, CZTS amd GaAs, which will be simulated with suggested method.

In the future, the stability issue involved in the QCRF based FDTD method will be studied more deeply for further developments of this model. Basically, an analytic stability achieved with the Kramers-Kronig consistent dispersion model such the QCRF model was recently studied in the paper [25], however numerical stability of the QCRF model has not been fully studied. Fortunately initial results indicate good performance in this thesis, however some of results caused numerical instability issues. Also, the complex rational function can be extended to quartic form and further. More poles allow for greater accuracy but it also consumes more computational cost. Finding the best trade off is another area for future study.

LIST OF REFERENCES

LIST OF REFERENCES

[1] P. Antognetti, G. Massobrio, "Semiconductor Device Modeling with SPICE", McGraw-Hill, Inc. NY, 1993.

[2] D. A. Antoniadis, S . E. Hansen, and R. W. Dutton, "SUPREM II - A program for IC Process Modeling and Simulation," Stanford Electronics Lab., Tech. Rep. 5019-2, June (1978).

[3] H. Lee, "Silicon based thin film solar cell technology," Magzine of the Korean Physics Society, pp. 15-19, (2008).

[4] D.L. Staebler and C.R. Wronski, "Reversible conductivity changes in discharge produced amorphous Si," *APL* 31, 292 (1977).

[5] J. Yang, and S. Guha, "Triple-junction amorphous silicon alloy solar cell with 14.6 percent initial and 13.0 percent stable conversion efficiencies," *APL* 70, 2975 (1997).

[6] D.E. Carlson and C.R. Wronski, "Amorphous silicon solar cell," *APL* 28, 671 (1976).

[7] W. Shockley and H. J. Queisser, "Detailed balance limit of efficiency of p-n junction solar cells," *Journal of Applied Physics*, vol. 32, no. 3, pp. 510-519, (1961).

[8] A. Taflove, *Computational Electrodynamics: The Finite Difference Time Domain Method*, 3rd ed., Norwood, MA: Artech House, (2005).

[9] S. D. Gedney, *Introduction to the Finite-Difference Time-Domain (FDTD) Method for Electromagnetics*, Morgan & Claypool Publishers, (2011).

[10] K.-Y. Jung, B. Donderici, and F. L. Teixeira, "Transient analysis of spectrally asymmetric magnetic photonic crystals with ferromagnetic losses," *Phys. Rev. B*, vol. 74, pp. 165207(1)-165207(11), Oct. (2006).

[11] K.-Y. Jung, S. Ju, and F. L. Teixeira, "Application of the modal CFS-PML-FDTD to the analysis of magnetic photonic crystal waveguides," *IEEE Microw. Wireless Compat. Lett.*, vol. 21, no. 4, pp. 179-181, Apr. (2011).

[12] I. Rekanos, "FDTD modeling of Havriliak-Negami media," *IEEE Microw. Wireless Compat. Lett.*, vol. 22, no. 2, pp. 49-51, Feb. (2012).

[13] K.-Y. Jung and F. L. Teixeira, "Multispecies ADI-FDTD algorithm for nanoscale three-dimensional photonic metallic structures," *IEEE Photon. Technol. Lett.*, vol. 19, no. 8, pp. 586-588, Apr. (2007).

[14] K.-Y. Jung, F. L. Teixeira, and R. M. Reano, "Au/SiO_2 nanoring plasmon waveguides at optical communication band," *J. Lightw. Technol.*, vol. 25, no. 9, pp. 2757-2765, Sep. (2007).

[15] V. E. do Nascimento, K.-Y. Jung, B.-H. V. Borges, and F. L. Teixeira, "A study of unconditionally stable FDTD methods for the modeling of metamaterials," *J. Lightw. Technol.*, vol. 27, no. 19, pp. 4241-4249, Oct. (2009).

[16] G. E. Jellison and F. A. Modine, "Parameterization of the optical functions of amorphous materials in the interband region," *Appl. Phys. Lett.* 69, 371 (1996).

[17] A.Fantoni and P. Pinho, "FDTD simulation of light propagation inside a-Si:H structures," *Mater. Res. Soc. Symp. Proc.* Vol. 1245 (2010).

[18] Vivian. E et al., "Improved red-response in thin film a-Si:H solar cells with soft-imprinted plasmonic back reflectors," *Appl. Phys. Lett.* 95, 183503 (2009).

[19] Aparajita Mandal and Partha Chaudhuri, "Size and period optimization of front patterned interacting metal nanoparticles for maximizing absorption of solar radiation in amorphous silicon thin films", *J. Opt.* 14 (2012).

[20] F. L. Teixeira, "Time-domain finite-difference and finite-element methods for Maxwell equations in complex media," *IEEE Trans. Antennas Propag.*, vol. 56, no. 8, pp. 2150-2166, Aug. (2008).

[21] Eldon L. Haines and A. Bruce Whitehead, "Pulse Height Defect and Energy Dispersion in Semiconductor Detectors," *Rev. Sci. Instrum.* 37, 190 (1966).

[22] A.Fantoni and P. Pinho, "FDTD simulation of light propagation inside a-Si:H structures," *Mater. Res. Soc. Symp. Proc.* Vol. 1245 (2010).

[23] W. C. Chew, *Waves and Fields in Inhomogeneous Media*, NewYork: IEEE Press, (1995).

[24] C. Gabriel, "Compilation of the dielectric properties of body tissues at RF and microwave frequencies," Brooks Air Force, Brooks City base, TX, Tech. Rep. AL/OE-TR-1996-0037, (1996).

[25] S. Ha, J. Cho, J. Choi, H. Kim, and K. -Y. Jung, "FDTD disperisve modeling of human tissues based on quadratic complex rational function," *IEEE Trans. Antennas Propag.*, to be published.

[26] W. C. Chew, *Waves and Fields in Inhomogeneous Media*, NewYork: IEEE Press, (1995).

[27] Gabriel, Camelia. "Compilation of the Dielectric Properties of Body Tissues at RF and Microwave Frequencies". *KING'S COLL LONDON (UNITED KINGDOM) DEPT OF PHYSICS*, 1996.

[28] J. Robinson and Y. Rahmat-Samii, "Particle swarm optimization in electromagnetics," *IEEE Trans. Antennas Propag.*, vol. 52, pp. 397-407, Feb. (2004).

[29] R. C. Eberhart and Y. Shi, "Particle swarm optimization: Developments, applications and resources," in *Proc. IEEE Congress on Evolutionary Computation*, (2001), pp. 81-86.

[30] A. Carlisle and G. Doizier, "An off-the-shelf PSO," in *ProcWorkshop Particl Swarm Optimization*, Indianapolis, IN, (2001).

[31] H. Chung, S. Ha, J. Cho, and K-Y. Jung, "Complex-Curve Fitting for Dispersive Media in FDTD Using Rational Function and Particle Swarm Optimization," *IEEE Trans. Antennas Propag.*, submitted (2013).

[32] E. C. Levi, "Complex-curve fitting," *IRE Trans. Automat. Contr.*, vol. 4, pp. 37-44, May (1959).

[33] Mulato et al., "Determination of thickness and optical constants of amorphous silicon films from transmittance data," *Appl. Phys. Lett.*, 77 (14), 2133 (2000).

[34] G. E. Jellison, Jr. and F. A. Modine, "Parameterization of the optical functions of amorphous materials in the interband region," *Appl. Phys. Lett.* 69, 371 (1996).

[35] E. D. Palik, Ed., "Handbook of Optical Constants of Solids." *Orlando, FL: Academic,* (1985).

[36] https://nanohub.org/tools/photonicsdb/.

[37] C. M. Herzinger, B. Johs, W. A. McGahan, J. A. Woollam, and W. Paulson Citation, "Ellipsometric determination of optical constants for silicon and thermally grown silicon dioxide via a multi-sample, multi-wavelength, multi-angle investigation," *J. Appl. Phys.* 83, 3323 (1998).

[38] H. Chung, J. Cho, S-G. Ha, S. Ju, and K-Y. Jung, "Accurate FDTD Dispersive Modeling for Concrete Materials," *ETRI Journal*, vol. 35, no. 5, Oct. (2013).

[39] W. C. Chew and W. Weedon, "A 3-D perfectly matched medium from modified Maxwell's equations with streched coordinates," *Microw. Opt. Technol. Lett.*, vol. 7, pp. 599-604, Sep. (1994).

[40] F. L. Texeira and W. C. Chew, "On causality and dynamic stability of perfectly mathced layers for FDTD simulations," *IEEE Trans. Microw. Theory Tech.*, vol. 47, no. 6, pp. 775-785, Jun. (1999).

[41] K.-Y. Jung, F. L. Teixeira, and R. Lee, "Complex envelope PML-ADI-FDTD method for lossy anisotropic dielectrics," *IEEE Antennas Wireless Propag. Lett.*, vol. 6, pp. 643-646, (2007).

[42] K.-Y. Jung, S. Ju, and F. L. Teixeira, "Two-stage perfectly matched layer for the analysis of plasmonic structures," *IEICE Trans. Electron.*, vol. E93-C, no. 8, pp. 1371-1374, Aug. (2010).

[43] D.K. Cheng, "Field and Wave Electromagnetics," 2nd Edition, *Addison-Wesley*, Reading, MA, (1989).

[44] Orfanidis, S. J., Electromagnetic Waves and Antennas, /emphRutgers University, 2008.

[45] Leo T. et al, "Enhanced photon management of thin-film silicon solar cells using inverse opal photonic crystals with 3D photonic bandgaps," *Advanced Optical Materials*, July 19, (2013).

[46] H. J. Queisser, K. Hubner, and W. Shockley, "Diffusion along Small-Angle Grain Boundaries in Silicon," *Phys. Rev.* 123. (1961)

[47] R. Brendel, M. Hirsch, R. Plieninger, and J.Werner, "Quantum efficiency analysis of thin-layer silicon solar cells with back surface fields and optical confinement," *IEEE Transactions on Electron Devices* 43, 1104-1113 (1996).

[48] T. Tiedje, E. Yablonovitch, G. D. Cody, and B. G. Brooks, "Limiting efficiency of silicon solar cells," *IEEE Transactions on Electron Devices* 31, 711-716 (1984)

[49] L. Zeng, P. Bermel, Y. Yi, N. Feng, B. A. Alamariu, C. Hong, X. Duan, J. Joannopoulos, and L. C. Kimerling, "Optimization of Textured Photonic Crystal Backside Reflector for Si Thin Film Solar Cells", *Materials Research Society Symposium Proceedings* 974E, CC2.6 (2006).

[50] M. Ghebrebrhan, P. Bermel, Y. Avniel, J. D. Joannopoulos, S. G. Johnson, "Global optimization of silicon photovoltaic cell front coatings", *Optics Express* 17, 7505 (2009)

[51] ASTMG173-03, Standard Tables for Reference Solar Spectral Irradiances: Direct Normal and Hemispherical on 37degree Tilted Surface (ASTM International, West Conshohocken, Pennsylvania, 2005).

[52] P. Bermel, C. Luo, L. Zeng, L. C. Kimerling, and J. D. Joannopoulos, "Improving thin-film crystalline silicon solar cell efficiencies with photonic crystals", *Optics Express* 15, 16986 (2007).

[53] http://nanohub.org/resources/adeptnpt

[54] http://ab-initio.mit.edu/wiki/index.php/Meep

[55] K. Yamamoto et al, "NOVEL HYBRID THIN FILM SILICON SOLAR CELL AND MODUZR," *3rd World Conference on Photovolraic Energy Conversion*, May, (2003).

[56] Keevers, M. J., et al. "10% efficiency CSG minimodules." *Proceedings of the 22nd European Photovoltaic Solar Energy Conference.* (2007).

[57] R. V. K. Chavali, John R. Wilcox, B. Ray, J. L. Gray and M. A. Alam, "A Diagnostic Tool for Analyzing the Current-Voltage Characteristics in a-Si/c-Si Heterojunction Solar Cells," *Proc. of 37th IEEE Photovoltaic Specialists Conference (PVSC)*, June 16-21, (2013).

[58] S. Dongaonkar, D. Wang, M. Frei, S. Mahapatra, and M. Alam, "On the Nature of Anomalous Shunt Leakage in Amorphous Silicon p-i-n Solar Cells," *IEEE Electron Device Letters* (2010).

[59] M. A. Kroon and R. A. C. M. M. van Swaaij, "Spatial effects on ideality factor of amorphous silicon pin diode," *J. Appl. Phys.* 90, 994 (2001).

[60] S. Wiesendanger, M. Zilk, T. Pertsch, F. Lederer, and C. Rockstuhl, "A path to implement optimized randomly textured surfaces for solar cells," *Appl. Phys. Lett.* 103, 131115 (2013).

[61] ASTMG173-03, *Standard Tables for Reference Solar Spectral Irradiances: Direct Normal and Hemispherical on 37 degree Tilted Surface* (ASTM International, West Conshohocken, Pennsylvania, 2005).

[62] S. Benagli, et al,"High-efficiency amorphous silicon devices on LPCVD-ZNO TCO prepared in industrial KAI-M R/D reactor," *24th European Photovoltaic Solar Energy Conference*, Hamburg, Sep (2009).

[63] Green, Martin A., et al. "Solar cell efficiency tables (version 39)." *Progress in photovoltaics: research and applications 20.1* (2011).

[64] http://pveducation.org/pvcdrom